Composite Structures 354 (2025) 118742

Contents lists available at ScienceDirect

Composite Structures

journal homepage: www.elsevier.com/locate/compstruct

Energy-based form-finding of reticulated shells accounting for eigenvalue buckling

Matteo Bruggi *, Carlo Guerini

Department of Civil and Environmental Engineering, Politecnico di Milano, 20133, Milano, Italy

ARTICLE INFO

Keywords:
Structural optimization
Force density method
Linear buckling
Reticulated shells
Stretching-dominated lattices
Additive manufacturing

ABSTRACT

A formulation of structural optimization that is based on the force density method is used to deal with the elastic design of stiff gridshells and of structural components made of stretching-dominated lattices. While most of the conventional approaches deal with plastic design, the complementary strain energy is used as objective function, whereas geometric and volume constraints are dealt with. The set of force densities that corresponds to the spatial geometry of minimum compliance is sought by using sequential convex programming. The formulation can be endowed with a smooth eigenvalue buckling constraint that is implemented to enforce a lower bound for the critical load. The implementation of the method is discussed, with special regard to the evaluation of the linear stiffness matrix and the initial stress matrix. Numerical simulations are shown, addressing reticulated shells subjected to gravity loads and a lightweight column-like element related to applications in additive manufacturing. The sensitivity of the optimal shape to the buckling constraint is assessed, depending on the required structural performance.

1. Introduction

Reticulated shells take their strength from their double curvature, being constructed from members that mainly undergo axial forces, i.e. stretching-dominated branches, see e.g. [1]. Among the approaches that can be used for the definition of the spatial location of their nodes, see e.g. [2–8], the "force density method" [9] can be resorted to when statically admissible solutions are sought in the form-finding process. This approach allows for defining the geometry of funicular networks of the loads by solving a system of linear equations. Its coefficient matrix depends on the prescription of suitable sets of force densities, i.e. ratios force-to-length in the branches of the network. Generally, when all force densities are identical, layouts are reasonably regular and may be adopted for a preliminary material-independent design of many funicular and anti-funicular structures. The idea was originally developed for cable-nets, but it was likewise extended to deal with the plastic design of gridshells, see e.g. [10], and, extensively, to investigate the self-equilibrated configuration of tensegrity structures, see e.g. [11–15]. The linear version of the force density method does not allow for directly incorporating local constraints, such as enforcements on length and tension limits of the elements. To this goal, constrained versions of the method may be used, resorting to iterative procedures that manage the nonlinearity introduced by the additional requirements. As pointed out e.g. in [16,17], no straightforward control of the coordinates of the free nodes can be operated. Ad hoc strategies to enforce the location of certain nodes of the net were proposed, among the others, in [16] searching for the optimal configurations of lightweight bridges by means of multi-objective genetic algorithms, in [18] working with the optimal design of geodesic tension trusses with uniform stress, and in [19] investigating a design framework for cable stayed/suspension bridges. Reference is also made to the natural force density method in [20] concerning the design of membrane elements and providing an insight of the concept of force density in relation to nonlinear finite element analysis.

It must be remarked that the force density method is well-suited for matrix-based implementation, and for coupling with gradient-based algorithms of structural optimization. If the force densities are adopted as optimization variables, the sensitivity of a few quantities of interest, such as the length and the tension of each bar, are available in the form of hessian matrices from the original work in [9]. In [21] it was shown that, working with the design of networks with fixed plan projection, the parameters governing the form-finding procedure consist of a reduced set of force densities. This approach, originally presented in the framework of limit analysis of masonry vaults, was further exploited to design reticulated shells of minimum load path [22]. Following [23], minimizing the total load path of a structure, which consists of the sum over the elements of the absolute value of the force times the length, corresponds directly to minimizing its weight in a

* Corresponding author.
E-mail address: matteo.bruggi@polimi.it (M. Bruggi).

https://doi.org/10.1016/j.compstruct.2024.118742
Received 3 June 2024; Received in revised form 18 October 2024; Accepted 24 November 2024
Available online 29 November 2024

fully stressed plastic design problem. An evolutionary algorithm and a hessian–based minimizer were adopted to retrieve optimal reticulated shells with given fixed projection. A constrained force density method was subsequently proposed in [24], combining the minimization of the total load path with control of the member lengths and of the spatial location of the unrestrained nodes, each one with three degrees of freedom. The arising nonlinear programming problem, comprising multiple constraints, was solved by means of an interior-point optimization algorithm. With reference to the form-finding of gridshells having prescribed horizontal projection, the work in [25] showed that, in simple cases, thrusts (i.e. horizontal components of the reaction) and coordinates of the nodes are linear in the force densities and in their reciprocal values, respectively. This suggests the adoption of methods of sequential convex programming that employ a different type of approximation depending on the sign of the gradient, see e.g. [26] with special regard to the Method of Moving Asympthotes (MMA) [27]. These solvers were especially conceived to deal with size optimization of elastic structures and are widely adopted to deal with multi-constrained problems of topology optimization at different scales, see e.g. [28–30]. Likewise, they may be conveniently used to cope with optimization problems whose state equation is the equilibrium in terms of force densities. Formulations of plastic design for networks with fixed plan projection were implemented in [25], for minimum thrust, and in [31], addressing a min–max problem to control the utilization of each element with respect to yielding and member buckling. The adoption of the so-called compliance as objective function, i.e. twice the strain energy at equilibrium [32], was used in conjunction with the force density method in [33], dealing with the design of plane and spatial trusses and resorting to sequential quadratic programming.

Instabilities are known to be a critical issue for reticulated shells, see in particular [34–36]. In addition to member buckling, local instabilities, which involve one or few nodes, and global instabilities, which affect the whole structure, may arise. Moreover, as discussed in [8], optimal shapes found by searching for solutions of minimum stress are prone to such type of collapse. Member buckling can be controlled by means of element constraints that affect slenderness and compressive stress, see e.g.[37]. Further stability considerations have been incorporated in the optimal design of gridshells following different strategies. Among the others, reference is made to the adoption of nominal forces in [36], using artificial loading cases to simulate the effect of imperfections within a plastic design formulation, and to the two-step procedure in [5], implementing the global linear buckling constraint proposed in [38]. Indeed, linear buckling is generally seen as a viable option to address the early stage design in truss geometry and topology optimization, see e.g. [39,40]. Nonlinear geometry optimization of domes is often related to the adoption of genetic algorithms, see e.g. [41].

Within the above framework, an energy-based form-finding strategy for reticulated shells is addressed in this contribution, stating structural optimization problems that resort to the force density method and are solved via sequential convex programming. The adoption of the force density method allows for searching among statically admissible layouts while taking advantage of the flexibility and quality of approximations peculiar to MMA. The complementary strain energy is adopted as objective function. A volume constraint is used to control the length of network, whose members have prescribed cross-section. Alternatively, local enforcements on subsets of the coordinates are employed as geometric constraints. The minimization unknowns consist of the whole set of force densities, such that the spatial location of the unrestrained nodes is affected only by a few prescriptions, if any. A new global constraint governing the value of the standard deviation of the element lengths, that means their slenderness, is introduced to regularize the problem without resorting to a more demanding set of local length constraints, see e.g. [24]. The minimization of the strain energy promotes recovering of the compatibility conditions, feature that is not shared by plastic design, where only statics is accounted for, see in particular the discussion in [42].

To include stability considerations in the form-finding process, the formulation for minimum compliance can be endowed with an eigenvalue buckling constraint. This enforces a prescribed lower bound for the critical load multiplier. Following [43], a smooth aggregation function is used to approximate the critical load depending on a few eigenvalues of the linear buckling problem. Dealing with topology optimization, this approach was shown to provide smoothness also in case of repeated eigenvalues and possible switching of the characteristic roots. It is here implemented and applied in the context of form-finding. The dependence of the stiffness matrix on the varying geometry of the network is handled in terms of the minimization unknowns by exploiting the formalism of the force density method, using results from the literature on tensegrity structures. However, unlike the case of the design of prestressed pin-jointed structures, the initial stress matrix requires the derivation of the elastic stress in the gridshell. Due to the implementation of the buckling constraint within a formulation of minimum strain energy, the adoption of the current set of force densities to approximate the stress regime is regarded as an option when constructing the initial stress matrix.

Numerical simulations are presented, concerning reticulated shells subjected to vertical loads and a column-like latticed element. Optimal shapes retrieved by the proposed energy-based form-finding methodology are shown, commenting on the sensitivity of the achieved solutions to the prescriptions of the eigenvalue buckling constraint. According to the achieved results, approximating the elastic force densities by the unknowns of the minimum strain energy problem may be an option for controlling the critical load multiplier without directly solving the elastic equilibrium, as generally required in alternative formulations [37]. This implies a reduction of the computational cost, including that required for the sensitivity computation.

It must be remarked that the proposed approach is conceived for gridshells and latticed structures in which nonlinear effects may be neglected provided that the critical load multiplier is reasonably large [44]. Reference is made e.g. to [45] concerning energy-based approaches to address the mechanical response of (tensegrity) structures for which different stable states exist.

The reminder of the paper is as follows. Section 2 presents the problem formulation, including a review of the force density method in case of partially and fully restrained nodes, fundamentals of the implemented optimization problems, and remarks on the solution procedure. Section 3 reports about numerical tests, whereas Section 4 concludes the paper addressing limitations and ongoing developments.

2. Problem formulation

The proposed approach exploits the "force density method" (FDM) [9] to retrieve networks that withstand the prescribed external loads with axial forces only, see Section 2.1. The arising equilibrium equations are firstly embedded in an energy-based minimization procedure, see Section 2.2. Then, the same formulation is endowed with an eigenvalue buckling constraints, see Section 2.3. The adopted gradient-based strategy is referred to in Section 2.4, whereas the sensitivity computation is given in Appendix.

2.1. The force density method

Given a Cartesian reference system $Oxyz$, a three-dimensional network consisting of m elements and n_s nodes is considered. The coordinates of the nodes are gathered in the arrays $\mathbf{x}_s$, $\mathbf{y}_s$, and $\mathbf{z}_s$, for the x, y, and z axes, respectively. The vector $\mathbf{x}_f$ collects the coordinates along the x axis of the nodes restrained in the same direction, whereas $\mathbf{x}$ gathers the x coordinate of the remaining set of nodes. The same definitions hold for the vectors $\mathbf{y}_f$ and $\mathbf{y}$, along with $\mathbf{z}_f$ and $\mathbf{z}$, considering the y

axis and the z axis, respectively. The topology of the spatial network is described by the connectivity matrix $\mathbf{C}_s$, whose entry are defined as:

$$C_{s\,ji} = \begin{cases} +1 & \text{if } i \text{ is the first node of the } j\text{-th element,} \\ -1 & \text{if } i \text{ is the second node of the } j\text{-th element,} \\ 0 & \text{otherwise,} \end{cases} \tag{1}$$

being $\mathbf{C}_h$ the subset which corresponds to the unrestrained nodes in the h direction, whereas $\mathbf{C}_{f\,h}$ refers to the restrained ones along the same axis. The vectors $\mathbf{u}$, $\mathbf{v}$, $\mathbf{w}$ store the difference in coordinates between the ends of each element along the x, y, and z axes, respectively:

$$\begin{aligned} &\mathbf{u} = \mathbf{C}_s\mathbf{x}_s = \mathbf{C}_x\mathbf{x} + \mathbf{C}_{fx}\mathbf{x}_f, \quad \mathbf{v} = \mathbf{C}_s\mathbf{y}_s = \mathbf{C}_y\mathbf{y} + \mathbf{C}_{fy}\mathbf{y}_f, \\ &\mathbf{w} = \mathbf{C}_s\mathbf{z}_s = \mathbf{C}_z\mathbf{z} + \mathbf{C}_{fz}\mathbf{z}_f. \end{aligned} \tag{2}$$

The vector $\mathbf{l}$ gathers the length of the branches of the network, being $l_j = \left(u_j^2 + v_j^2 + w_j^2\right)^{1/2}$ the length of the jth branch. Upon introduction of the diagonal matrices $\mathbf{U} = \text{diag}(\mathbf{u})$, $\mathbf{V} = \text{diag}(\mathbf{v})$, $\mathbf{W} = \text{diag}(\mathbf{w})$, and $\mathbf{L} = \text{diag}(\mathbf{l})$, the equilibrium equations for the unrestrained nodes of the network read:

$$\mathbf{C}_x^T\mathbf{U}\mathbf{L}^{-1}\mathbf{s} = \mathbf{p}_x, \quad \mathbf{C}_y^T\mathbf{V}\mathbf{L}^{-1}\mathbf{s} = \mathbf{p}_y, \quad \mathbf{C}_z^T\mathbf{W}\mathbf{L}^{-1}\mathbf{s} = \mathbf{p}_z, \tag{3}$$

where $\mathbf{s}$ gathers the forces in the branches, $\mathbf{p}_x$, $\mathbf{p}_y$, $\mathbf{p}_z$ collect the components along the Cartesian axes of the point loads at the unrestrained nodes, and the following relations have been used:

$$\frac{\partial \mathbf{l}^T}{\partial \mathbf{x}} = \mathbf{C}_x^T\mathbf{U}\mathbf{L}^{-1}, \quad \frac{\partial \mathbf{l}^T}{\partial \mathbf{y}} = \mathbf{C}_y^T\mathbf{V}\mathbf{L}^{-1}, \quad \frac{\partial \mathbf{l}^T}{\partial \mathbf{z}} = \mathbf{C}_z^T\mathbf{W}\mathbf{L}^{-1}. \tag{4}$$

The force density vector, i.e. the vector collecting the ratio force to length of the branches of the network is defined as $\mathbf{q} = \mathbf{L}^{-1}\mathbf{s}$, being $q_j = s_j/l_j$. Introducing $\mathbf{Q} = \text{diag}(\mathbf{q})$, Eq. (3) becomes:

$$\begin{aligned} &\mathbf{C}_x^T\mathbf{Q}\mathbf{C}_x\mathbf{x} + \mathbf{C}_x^T\mathbf{Q}\mathbf{C}_{fx}\mathbf{x}_f = \mathbf{p}_x, \quad \mathbf{C}_y^T\mathbf{Q}\mathbf{C}_y\mathbf{y} + \mathbf{C}_y^T\mathbf{Q}\mathbf{C}_{fy}\mathbf{y}_f = \mathbf{p}_y, \\ &\mathbf{C}_z^T\mathbf{Q}\mathbf{C}_z\mathbf{z} + \mathbf{C}_z^T\mathbf{Q}\mathbf{C}_{fz}\mathbf{z}_f = \mathbf{p}_z. \end{aligned} \tag{5}$$

For any given set of $\mathbf{q}$ and $\mathbf{x}_f$, $\mathbf{y}_f$, $\mathbf{z}_f$, along with prescribed loads, Eq. (5) allows for calculating the coordinates of the unrestrained nodes of the funicular network. It is worth remarking that the above equations are linear and uncoupled for the determination of $\mathbf{x}$, $\mathbf{y}$, and $\mathbf{z}$. Firstly adopted in the form-finding of funicular and anti-funicular networks, see also [46], they are extensively applied in the design of prestressed pin-jointed structures comprising both compressive and tensile elements, see e.g. [11,12].

2.2. Elastic design of reticulated shells

A few objective functions may be selected to optimize the location of the nodes of a reticulated shell, given the equilibrium condition stated in Eq. (5). They generally refer to plastic design, see in particular the case of the load–path function to find the lightest design for a given stress in all the branches of the gridshell [22,24]. In this contribution, the elastic design is addressed considering the strain energy as objective function [32,33]. This objective function is commonly used when dealing with the design of lightweight structural components for construction, see e.g. [47,48]. Dealing with a linear elastic material with Young's modulus E, it equals the complementary strain energy U_c. Hence, for a reticulated shell where all the branches are made of profiles with the same cross-section, and A is the area, it may be computed as:

$$U_c = \frac{1}{2}\sum_{j=1}^{m}\left(\frac{s_j}{A}\frac{s_j}{EA}Al_j\right) = \frac{1}{2EA}\mathbf{s}^T\mathbf{L}\mathbf{s} = \frac{1}{2EA}\mathbf{q}^T\mathbf{L}^3\mathbf{q}. \tag{6}$$

To mimic the classical volume-constrained minimum compliance problem [32], a length-constrained minimum strain energy problem is formulated adopting the force densities in $\mathbf{q}$ as minimization unknowns. It is stated as:

$$\begin{cases} \min_{\mathbf{q}} \; U_c & \text{(a)} \\ \text{s.t.} \;\; \mathbf{C}_x^T\mathbf{Q}\mathbf{C}_x\mathbf{x} + \mathbf{C}_x^T\mathbf{Q}\mathbf{C}_{fx}\mathbf{x}_f = \mathbf{p}_x, & \\ \quad\;\; \mathbf{C}_y^T\mathbf{Q}\mathbf{C}_y\mathbf{y} + \mathbf{C}_y^T\mathbf{Q}\mathbf{C}_{fy}\mathbf{y}_f = \mathbf{p}_y, & \text{(b)} \\ \quad\;\; \mathbf{C}_z^T\mathbf{Q}\mathbf{C}_z\mathbf{z} + \mathbf{C}_z^T\mathbf{Q}\mathbf{C}_{fz}\mathbf{z}_f = \mathbf{p}_z, & \\ \quad\;\; \sum_{j=1}^{m} l_j \le l_{t,max}, & \text{(c)} \\ \quad\;\; \frac{1}{m}\mathbf{l}^T\mathbf{l} - \left(\sum_{j=1}^{m} l_j\right)^2 \le l_{sd,max}^2, & \text{(d)} \end{cases} \tag{7}$$

where $l_{t,max}$ is the maximum allowed total length of the network and $l_{sd,max}$ is the maximum allowed standard deviation of the element lengths. A reticulated shell that can withstand external loads with axial forces only is prescribed by Eq. (7b). The global enforcement in Eq. (7c) is used to govern the available amount of material, whereas that in Eq. (7d) aims at limiting the variation of the length of the members about the mean value. This allows to control, although in a weak sense, the slenderness of the branches against member buckling, and to provide a regularization of the optimization problem, see in particular [49,50].

In case of statically indeterminate structures, the set of force densities $\mathbf{q}$ that corresponds to the same overall geometry is not unique. Based on the principle of minimum complementary energy, assuming that no displacement occurs at the supports, Eq. (7) is expected to retrieve the set of force densities that corresponds to the solution of the linear elastic equilibrium $\mathbf{q}_L$, provided that such a solution is not jeopardized by the constraints in Eqs. (7c-d). Indeed, among all possible stress states which satisfy the equilibrium of a given structure, the state which fulfills the compatibility conditions will make the complementary energy assume a minimum value. If the supports have not moved, the work done by the applied loads during stress changes is null and the complementary energy coincides with the complementary strain energy of Eq. (6). This is known as Castigliano's principle of least works, see e.g. [51].

It is remarked that the formulation in Eq. (7) may be endowed with local constraints to control the geometry of the network, governing components of the vectors $\mathbf{x}$, $\mathbf{y}$, $\mathbf{z}$ and $\mathbf{l}$, and its stress regime, controlling entries of $\mathbf{s}$, see in particular [31]. For instance, in one of the examples of the numerical section, a modified version of the formulation in Eq. (7) will be used, replacing (7c) with constraints of the type:

$$z_{i_c} \ge z_{i_c}^{min} \quad \text{for} \;\; i_c = 1 \ldots n_{cz}. \tag{8}$$

This is done with the aim of enforcing a minimum value $z_{i_c}^{min}$ for the elevation of the i_c-th of a limited number of nodes n_{cz}, while disregarding the control on the employed amount of material.

2.3. Including an eigenvalue problem for global stability

A nonlinear finite element approach should be preferably adopted to investigate structural stability for the vector load $\mathbf{p} = [\mathbf{p}_x\,\mathbf{p}_y\,\mathbf{p}_z]^T$. However, when only small displacements and deformations occur before an instability point is reached, the first load level for which a structural system becomes unstable can be preliminary investigated by performing a so-called linear buckling analysis, see e.g. [52]. An eigenvalue problem is formulated as:

$$[\mathbf{K}_L + \lambda\hat{\mathbf{K}}_\sigma]\mathbf{\Phi} = \mathbf{0}, \tag{9}$$

where $\mathbf{K}_L$ is the linear stiffness matrix and $\hat{\mathbf{K}}_\sigma$ is the restriction of the initial stress (or geometric) matrix $\mathbf{K}_\sigma$ to the linear part of the displacements $\mathbf{d}_L$, i.e. $\hat{\mathbf{K}}_\sigma = \mathbf{K}_\sigma(\mathbf{d}_L)$ with $\mathbf{K}_L\mathbf{d}_L = \mathbf{p}$. The smallest eigenvalue retrieved in the solution of Eq. (9) yields the critical load factor λ_c, such that $\lambda_c\mathbf{p}$ is the first load level for which the structural system becomes unstable. The eigenvector $\mathbf{\Phi}$ that is computed from Eq. (9) for λ_c gives the shape of the relevant failure mode.

The literature of tensegrity structures provides the analytical forms of $\mathbf{K}_L$ and $\mathbf{K}_\sigma$ for spatial networks of bars exploiting the formalism of the force density method. In [53], the second-order increment of the total potential energy due to small deformations is investigated to derive the global tangent stiffness matrix of a (prestressed) pin-jointed structure. The linear part $\mathbf{K}_L$ depends on geometry realization as well as member axial stiffness, i.e. Young's modulus of the material and cross-section area of the branches. The geometric matrix $\mathbf{K}_\sigma$ is dependent on the connectivity of the branches and the stress regime.

By generalizing to the case of reticulated shells with nodes that admit partial restraints, while specializing to the case of equal cross-section and material for all the branches, the matrices in Eq. (9) can be computed as:

$$\mathbf{K}_L = \mathbf{B}\bar{\mathbf{K}}\mathbf{B}^T, \quad \text{where } \mathbf{B} = \begin{bmatrix} \mathbf{C}_x^T\mathbf{U}\mathbf{L}^{-1} \\ \mathbf{C}_y^T\mathbf{V}\mathbf{L}^{-1} \\ \mathbf{C}_z^T\mathbf{W}\mathbf{L}^{-1} \end{bmatrix} \text{and } \bar{\mathbf{K}} = EA\mathbf{L}^{-1}, \tag{10}$$

and

$$\hat{\mathbf{K}}_\sigma = \begin{bmatrix} \mathbf{C}_x^T\mathbf{Q}_L\mathbf{C}_x & \mathbf{0} & \mathbf{0} \\ \mathbf{0} & \mathbf{C}_y^T\mathbf{Q}_L\mathbf{C}_y & \mathbf{0} \\ \mathbf{0} & \mathbf{0} & \mathbf{C}_z^T\mathbf{Q}_L\mathbf{C}_z \end{bmatrix}, \quad \text{where } \mathbf{Q}_L = \text{diag}(\mathbf{q}_L). \tag{11}$$

Recalling that $\mathbf{q}_L$ is the set of force densities that corresponds to the solution of the linear elastic equilibrium $\mathbf{K}_L\mathbf{d}_L = \mathbf{p}$, one has:

$$\mathbf{q}_L = \mathbf{L}^{-1}\bar{\mathbf{K}}\mathbf{B}_x^T\mathbf{d}_L. \tag{12}$$

It is remarked that, for any network with prescribed connectivity of the members and given axial stiffness, $\mathbf{K}_L$ in Eq. (10) depends on $\mathbf{q}$ only, whereas $\hat{\mathbf{K}}_\sigma$ is written in Eq. (11) as a function of $\mathbf{q}_L$.

Since $\mathbf{K}_L$ is positive definite when kinematically determinate structures are dealt with, the problem in Eq. (9) is generally re-written as [54]:

$$[\hat{\mathbf{K}}_\sigma + \mu\mathbf{K}_L]\boldsymbol{\Phi} = \mathbf{0}, \tag{13}$$

where the first load level for which the structural system becomes unstable corresponds to the largest eigenvalue $\mu_1 = 1/\lambda_c$. The Kreisselmeier-Steinhauser aggregation function [55] is used to construct a smooth approximation of μ_1 involving a certain number of eigenvalues. One has:

$$J_{KS}(\boldsymbol{\mu}) = \mu_1 + \frac{1}{\rho}\ln\sum_{e=1}^{n_e} e^{\rho(\mu_e-\mu_1)}, \tag{14}$$

providing, when $\rho \geq 1$, an upper bound for μ_1 (i.e. a lower bound for $\lambda_c = 1/\mu_1$) over the largest n_e eigenvalues arranged in the vector $\boldsymbol{\mu} = [\mu_1\ \mu_2\ \ldots\ \mu_e\ \ldots\ \mu_{n_e}]^T$. Eq. (14) has been recently employed in topology optimization with linearized buckling criteria [43,56], proving effective in handling possible switching of the characteristic roots and in preserving smoothness of its derivative also in case of repeated eigenvalues [57].

Embedding the above stability considerations within the problem in Eq. (7), one gets:

$$\begin{cases} \min_{\mathbf{q}}\ U_c & \text{(a)} \\ \text{s.t.}\ \ \mathbf{C}_x^T\mathbf{Q}\mathbf{C}_x\mathbf{x} + \mathbf{C}_x^T\mathbf{Q}\mathbf{C}_{fx}\mathbf{x}_f = \mathbf{p}_x, & \\ \qquad \mathbf{C}_y^T\mathbf{Q}\mathbf{C}_y\mathbf{y} + \mathbf{C}_y^T\mathbf{Q}\mathbf{C}_{fy}\mathbf{y}_f = \mathbf{p}_y, & \text{(b)} \\ \qquad \mathbf{C}_z^T\mathbf{Q}\mathbf{C}_z\mathbf{z} + \mathbf{C}_z^T\mathbf{Q}\mathbf{C}_{fz}\mathbf{z}_f = \mathbf{p}_z, & \\ \qquad \mathbf{K}_L\mathbf{d}_L = \mathbf{p}, & \text{(c)} \\ \qquad [\hat{\mathbf{K}}_\sigma + \mu\mathbf{K}_L]\boldsymbol{\Phi} = \mathbf{0}, & \text{(d)} \\ \qquad J_{KS}(\boldsymbol{\mu}) \leq \frac{1}{\lambda_{c,min}}, & \text{(e)} \\ \qquad \sum_{j=1}^m l_j \leq l_{t,max}, & \text{(f)} \\ \qquad \frac{1}{m}\mathbf{l}^T\mathbf{l} - \left(\sum_{j=1}^m l_j\right)^2 \leq l_{sd,max}^2. & \text{(g)} \end{cases} \tag{15}$$

In Eq. (15e), $\lambda_{c,min}$ is the target minimum critical load factor, whose inverse is the enforced upper limit for $J_{KS}(\boldsymbol{\mu})$. The evaluation of $J_{KS}(\boldsymbol{\mu})$ requires the solution of the eigenvalue problem in Eq. (15d) to compute the largest n_e eigenvalues. This in turn calls for the solution of the elastic equilibrium in Eq. (15c) to assemble the initial stress matrix $\hat{\mathbf{K}}_\sigma$.

2.4. Numerical implementation

The minimization problems in Eqs. (7) and (15) include a limited number of constraints, either global or aggregated, for an efficient numerical treatment. They are solved by means of the Method of Moving Asympthotes (MMA) [27], see the discussion in Section 1 and previous applications in conjunction with the force density method in [25,31,58]. A nested analysis and design approach is adopted, meaning that, at each iteration, the equilibrium equations and the eigenvalue problem, if any, are solved for the current set of optimization variables. The evaluation of the objective function (o.f.), the inequality constraints and their gradients is performed accordingly. As shown in Appendix, the required sensitivities may be computed elaborating on the derivation of the Jacobian matrices originally presented in [9]. A flowchart of the procedure outlined above is given in Fig. 1, referring to the solution of the optimization problem in Eq. (15).

Since minimizing the strain energy goes in the direction of restoring compatibility, see Section 2.2, an approximation will be investigated in the numerical simulations when dealing with the formulation in Eq. (15). Denoting by $\tilde{\mathbf{K}}_\sigma$ the geometric matrix of Eq. (11) evaluated for $\mathbf{q}$ instead of $\mathbf{q}_L$, the eigenvalue problem in Eq. (15e) will be solved replacing $\hat{\mathbf{K}}_\sigma$ with $\tilde{\mathbf{K}}_\sigma$. Using this approximation, one skips the solution of the elastic equilibrium in Eq. (15c), as well as that of any additional adjoint problem of the type in Eq. (A.6) to compute the sensitivity of the eigenvalues, see Appendix.

Adopting the force density method instead of the finite element method implies that form-finding is operated by searching among networks that fulfill equilibrium (while generally dropping the compatibility requirement). Indeed, when the force densities are used as minimization unknowns, statically admissible networks are handled at each iteration because of the system in Eq. (5), which is linear and uncoupled in the nodal coordinates $\mathbf{x}$, $\mathbf{y}$, $\mathbf{z}$. This would not be the case, for instance, with a form-finding approach relying on the elastic equilibrium and adopting the nodal coordinates as minimization unknowns.

Eq. (15) combines the use of the force density method with the enforcement of a linear buckling constraint, for which $\mathbf{q}_L$ is required. As outlined above, the minimum energy problem promotes recovery of the compatibility requirement (working with statically admissible networks). Replacing $\mathbf{q}_L$ with $\mathbf{q}$ in the evaluation of the initial stress matrix is an approximation that avoids resorting e.g. to the finite element method for the solution of the linear elastic equilibrium. The validity of this approximation, aimed at reducing the computational cost, will be discussed in Section 3, using a finite element code for comparison.

3. Numerical examples

A few numerical examples are addressed to test the energy-based formulation of Section 2.2 and that in Section 2.3 accounting for eigenvalue buckling. In structural design and optimization of steel structures, see e.g. [59], first order analyses may be relied upon if deformations caused by an increase of the internal forces or any other change of structural behavior can be neglected. According to [44] this condition may be assumed to be fulfilled in case $\lambda_{c,min} = 10$ and $\lambda_{c,min} = 15$, for elastic and plastic analyses, respectively. Different prescriptions on $\lambda_{c,min}$ will be considered next to assess the sensitivity of the minimum compliance design to the eigenvalue buckling constraint.

For all the examples investigated next the number of eigenvalues considered in the aggregation function of Eq. (14) is $n_e = 6$, implementing $\rho = 1000$. Following [43], a large value of the aggregation parameter ρ has been adopted to preserve accuracy in the approximation of the critical load multiplier, see also the discussion in [60] concerning the stability of the implemented form of the aggregation function. However, the use of too large values of the control parameter should be avoided, aiming at preventing numerical issues in the

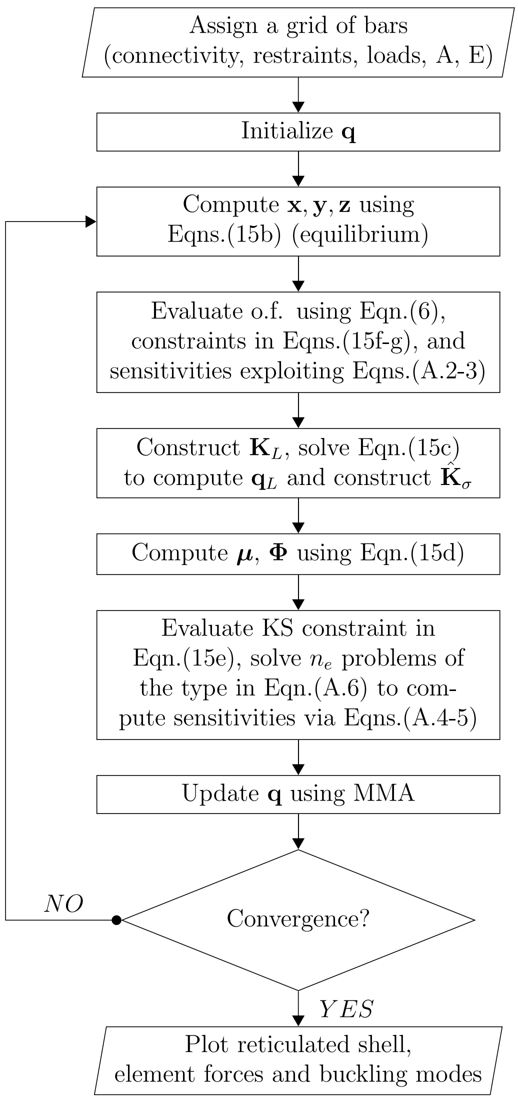

Fig. 1. Flowchart of the general approach for the solution of the optimization problem in Eq. (15).

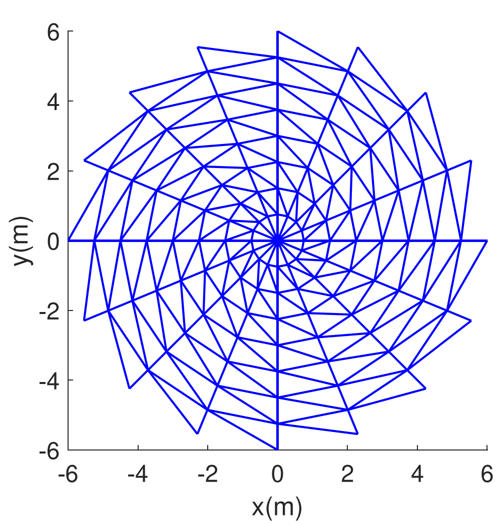

Fig. 2. Connectivity of the members of a Schwedler dome.

derivation operation that would affect convergence of the optimization algorithm.

The minimization of the strain energy aims at selecting the stiffest design among statically admissible solutions for a given set of requirements. The layouts presented next are characterized by non-singular stiffness matrices, meaning that all of them are completely restrained structures. It must be remarked that the kinematic determinacy of the retrieved solutions mainly depends on the connectivity of the selected grids. Indeed, no direct enforcement has been implemented to this goal, see in particular [53].

3.1. A dome

A dome spanning an area with $r = 6$ m is considered. The connectivity of a so-called Schwedler dome is investigated, which consists in the intersecting ribs, rings, and diagonal elements represented in Fig. 2, see e.g. [61]. The vertical load per unit of plan projection is 3 kN/m^2. The z axis is the vertical one. All the nodes along the perimeter are restrained in the three Cartesian axes. The maximum allowed total length of the network is $l_{t,max} = 1.075 \cdot l_{t,0} = 430$ m, being $l_{t,0} = 400$ m the total length of the members in the plan grid represented in Fig. 2. A profile of the type CHS 48.3/2.6 is assumed for all the branches of the reticulated shell, considering Young's modulus $E = 210$ GPa. The maximum allowed standard deviation of the element lengths is $l_{sd,max} = 0.4$ m.

It must be remarked that the system in Eq. (5) remains linear if the load vector is design-independent, meaning that the problem in Eqs. (7) and (15) must be solved at constant load. A first run is performed considering nodal forces that are computed according to the tributary area of the initial grid. The starting guess consists of a uniform distribution of compressive force densities throughout the network. Then, an iterative procedure is implemented, by updating the load vector after each optimization run, while adopting the current optimal distribution of force densities to initialize the subsequent step. The final solution is characterized by a relative variation in the minimization variables (with respect to the previous optimization run) that is less than 10^{-3}. In this contribution, gravity loads are dealt with. This means that the lines of action of the nodal forces remain vertical throughout the set of optimization runs, whereas the point of application of each nodal force is updated at the end of each design step. The same procedure could be adopted to handle loading conditions for which an update in the direction of the line of action of each force is required, see follower loads. Regardless of the loading scenario, the constraints in Eqs. (7d) and (15g) can be used to prevent the arising of abrupt design changes between two subsequent optimization runs.

The length-constrained minimum compliance design found using Eq. (7) is presented in Fig. 3. The value of the strain energy at converge is $U_c = 122.31$ Nm. The plan projection of the optimal solution is remarkably different from that shown in Fig. 2, exhibiting similarities with Michell structures [62] and lamella domes, see also [63]. The degree of statically indeterminacy is 13. This may be derived looking at the difference between the number of unknowns and the rank of the coefficient matrix for the linear system in Eq. (3), 352 and 339 respectively. In Fig. 3, a map of the forces in the branches of the network is given, plotting the entries of $\mathbf{s} = \mathbf{L}\mathbf{q}$, where the vector of the minimization unknowns $\mathbf{q}$ is that found at convergence and $\mathbf{L}$ stores the final lengths. As discussed in Section 2.2, a good match is expected with the values found via an elastic solution. This has been checked by using a commercial finite element analysis code [64], retrieving the same range of forces in the branches of the anti-funicular network ($s_{min} = -12.96$ kN, $s_{max} = -0.07$ kN). The maximum utilization factor, considering the Perry-Robertson failure criteria [65] for a material with yielding stress $\sigma_y = 235$ GPa and lack of straightness of the jth bar equal to $10^{-3} \cdot l_j$, is $0.31 \le 1$, whereas the slenderness of the bars ranges between 30 and 125.

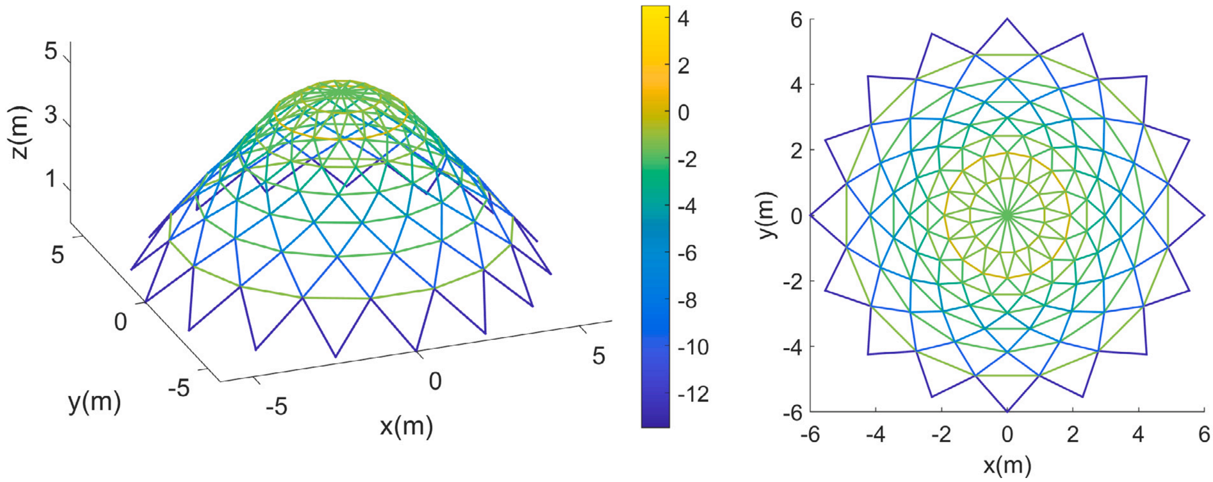

Fig. 3. Minimum compliance design of a dome ($U_c = 122.31$ Nm): optimal layout with map of the forces in the branches (in kN, $s_{min} = -12.96$ kN, $s_{max} = -0.07$ kN), in two views.

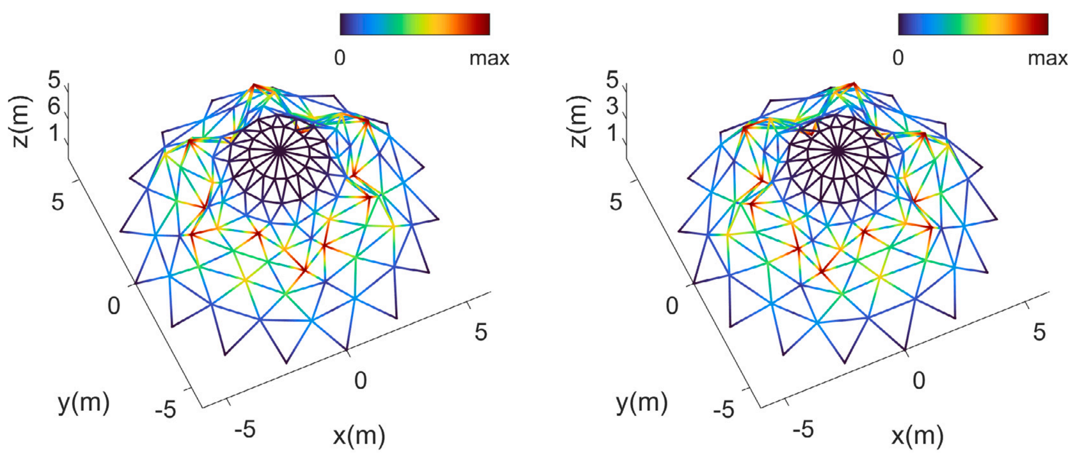

Fig. 4. Two eigenmodes associated to the critical load multiplier $\lambda_c = 9.160$ for the minimum compliance design of a dome. The color maps represent the amplitude of the buckling shapes.

Even though the local utilization factor is far lower than the threshold, the critical load multiplier is slightly below the level suggested by technical codes to rely on first order analyses [44]. Performing a linear buckling analysis of the achieved optimal structure, $\lambda_c = 9.160$ is found, both working with $\hat{\mathbf{K}}_\sigma$ and $\tilde{\mathbf{K}}_\sigma$, see Section 2.4. Two eigenmodes associated to the repeated multiplier $\lambda_c = \lambda_1 = \lambda_2$ are represented in Fig. 4. They involve almost all the dome, except for the region at the crown. In Table 1, the inverses of the largest n_e eigenvalues of the problem in Eq. (13) are shown and compared to the relevant values found via the commercial FEA code. A very good agreement is found, further assessing the implementation of the proposed energy-based procedure.

The formulation in Eq. (15) is used to investigate optimal layouts with an improved performance in terms of critical load. The optimization is initialized by adopting the previous solution as the starting guess. The same values $l_{t,max}$ and $l_{sd,max}$ are implemented. At first, the optimization is run for $\lambda_{c,min} = 20$. The achieved optimal design is reported in Fig. 5(left). A map of the forces acting in the branches of the network according to the entries of $\mathbf{q}$ at convergence is given. The eigenmode corresponding to the critical load $\lambda_c = 20.491$ is represented in Fig. 5(right). One has $\lambda_c \geq \lambda_{c,min}$ because of the peculiar behavior of the adopted aggregation function. At the cost of a minor increase in terms of objective function U_c and intensity of the forces s_{min} and s_{max}, a fully-compressed network is retrieved having twice the critical load of the solution in Fig. 3. Minor modifications in the shape of the dome may be reported, see also Fig. 7.

A further numerical investigation is performed implementing the eigenvalue buckling constraint for $\lambda_{c,min} = 50$. The optimal shape found by the minimization algorithm is depicted in Fig. 6(left), providing the force map retrieved from the values in $\mathbf{q}$ at convergence. The eigenmode corresponding to the critical load $\lambda_c = 54.286$ is represented in Fig. 6(right). With respect to the design achieved for $\lambda_{c,min} = 20$, a more rounded shape is retrieved is this case. To preserve the overall length, the elevation at the crown is lower, see Fig. 7. When the stricter prescription on λ_c is adopted, half of the rings are tensile-stressed ($s_{max} = 4.51$ kN), whereas s_{min} does not remarkably change. Notwithstanding a further increase in the value of the objective function at convergence, the maximum vertical displacement under the effect of the prescribed loads is less than 2 mm.

Both for $\lambda_{c,min} = 20$ and for $\lambda_{c,min} = 50$, the formulation in Eq. (15) was run using $\tilde{\mathbf{K}}_\sigma$ to approximate $\hat{\mathbf{K}}_\sigma$. At convergence, the vector of the minimization unknowns $\mathbf{q}$ was found to match $\mathbf{q}_L$ of Eq. (12), i.e. the vector gathering the force densities after an elastic solution. A very good agreement may be reported looking at Table 1, where the values $\lambda_e = 1/\mu_e$ from the results of the implemented procedure are reported along with those found using the commercial FEA code. The difference between pairs of values does not exceed 0.5%.

In Fig. 8, history plots of the objective function and of the feasibility of the constraints are reported for the buckling-constrained optimization problem enforcing $\lambda_{c,min} = 20$. At each iteration, the latter quantity accounts for the maximum value of the ratios left-hand-side to right-and-side for the set of constraints in Eqs. (15e-g). The picture on the

Table 1
Design of a dome for minimum compliance and different assumptions on the enforcement of $\lambda_{c,min}$: values $\lambda_e = 1/\mu_e$ for $e = 1 \ldots n_e$ computed using the proposed method vs. FEA via commercial code (*in italic*).

Design	λ_1	λ_2	λ_3	λ_4	λ_5	λ_6
min U_c (Fig. 3)	9.160	9.160	10.448	10.448	10.571	10.571
	9.166	*9.166*	*10.455*	*10.455*	*10.580*	*10.580*
min U_c, $\lambda_{c,min} = 20$ (Fig. 5)	20.491	20.491	20.692	20.693	21.781	22.503
	20.532	*20.532*	*20.732*	*20.732*	*21.837*	*22.548*
min U_c, $\lambda_{c,min} = 50$ (Fig. 6)	54.286	54.286	54.343	54.343	56.789	56.789
	54.489	*54.489*	*54.588*	*55.588*	*56.963*	*56.963*

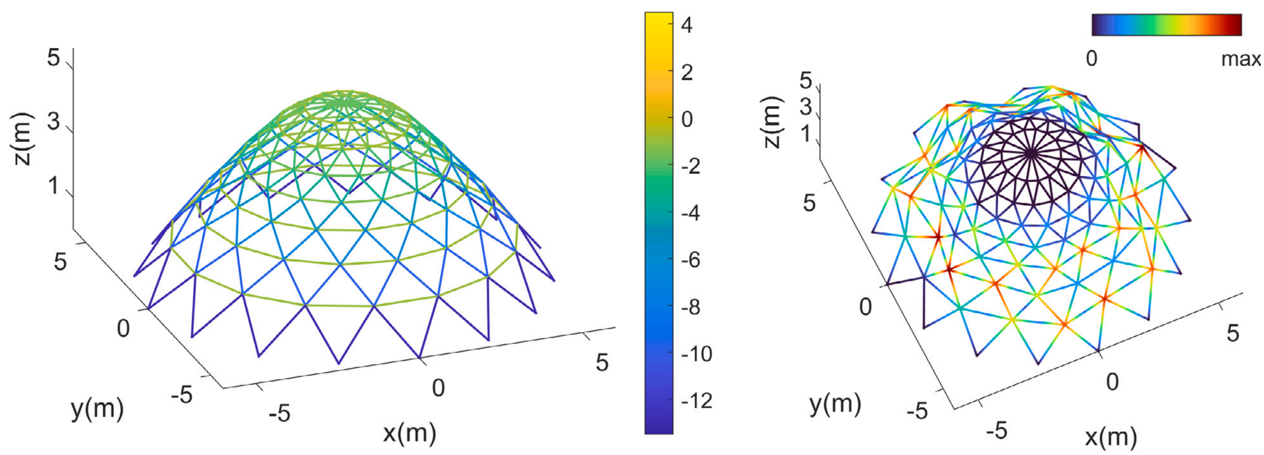

Fig. 5. Design of a dome for minimum compliance and $\lambda_{c,min} = 20$ ($U_c = 123.84$ Nm): optimal layout with map of the force in the branches (in kN, $s_{min} = -13.01$ kN, $s_{max} = -0.78$ kN, left); relevant buckling mode at $\lambda_c = 20.491$ (right).

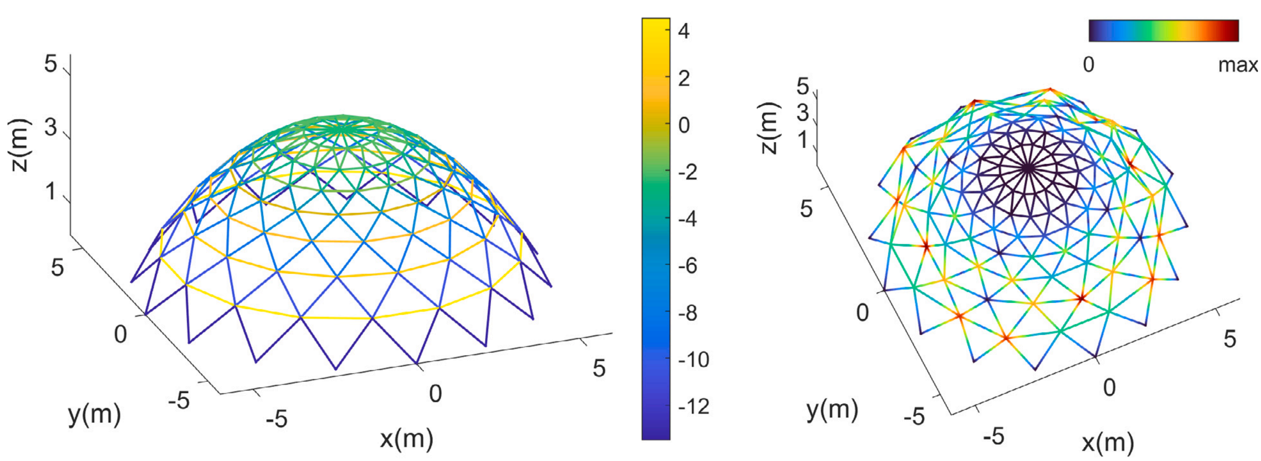

Fig. 6. Design of a dome for minimum compliance and $\lambda_{c,min} = 50$ ($U_c = 146.46$ Nm): optimal layout with map of the force in the branches (in kN, $s_{min} = -13.41$ kN, $s_{max} = 4.51$ kN, left); relevant buckling mode at $\lambda_c = 54.286$ (right).

left refers to the first run (which is initialized using the distribution of force densities in Fig. 3), whereas that on the right concerns the second run (which is performed after an update of the tributary area of each node and is initialized using the previous solution). In both cases, the algorithm starts from an unfeasible point, meaning that there exists at least one constraint that is violated, see in particular Eq. (15e). In the subsequent iterations, optimal values of the minimization unknowns are derived. The second run is characterized by less iterations, along with a reduced range of variation for the value of the feasibility of the constraints recorded throughout the run. This trend also applies to the subsequent steps, until convergence of the iterative optimization procedure.

In Fig. 9, history plots are given for the buckling-constrained optimization problem enforcing $\lambda_{c,min} = 50$. Again, the picture on the left refers to the first run (which is initialized as in the previous case), whereas that on the right addresses the second run (after an update of the tributary area of each node, using the solution of the first run as the starting guess). The comments already given for the curves found in the previous case apply.

It must be finally remarked that the proposed approach is limited to linear modeling, including linear buckling. As already mentioned, building codes consider the possibility of neglecting nonlinear effects provided that the critical load multiplier is reasonably large. Indeed, the adopted eigenvalue-based constraint is conceived to enforce such a condition by operating on the input parameter $\lambda_{c,min}$. However, there exist structural types for which geometric nonlinearities cannot be disregarded, see e.g. the case of reticulated domes acted upon by lateral forces. In this regard, the optimization problem should incorporate one of the geometrically nonlinear stability constraints reviewed by [66] in the context of topology optimization. A direct approach could be

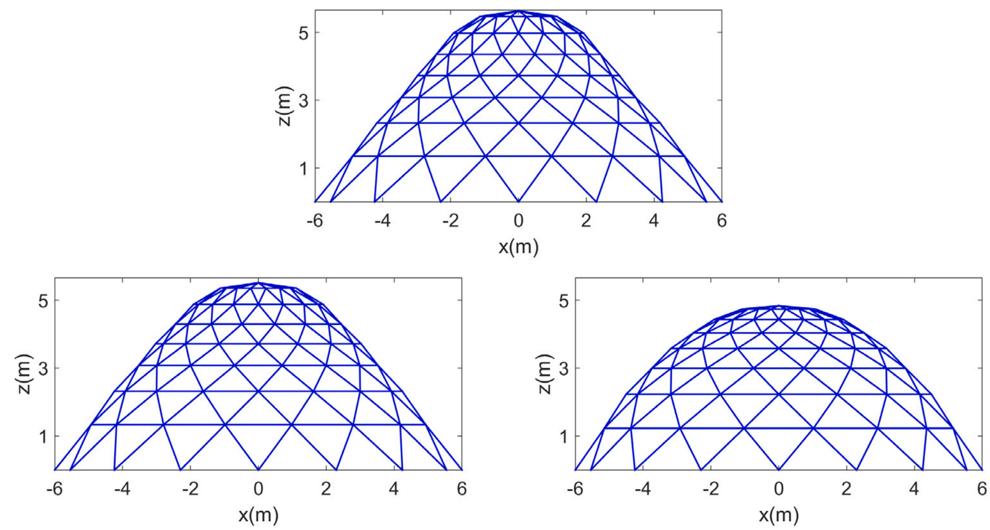

Fig. 7. Design of a dome for minimum compliance and different prescription on $\lambda_{c,min}$: side view of the optimal layout with no control of $\lambda_{c,min}$ (top), for $\lambda_{c,min} = 20$ (bottom left) and for $\lambda_{c,min} = 50$ (bottom right).

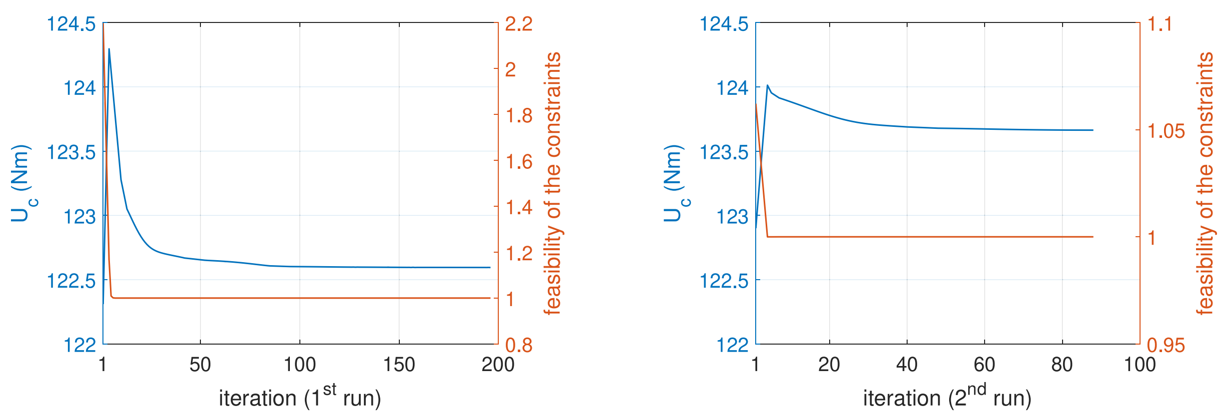

Fig. 8. Design of a dome for minimum compliance and $\lambda_{c,min} = 20$: history plot of the objective function and of the feasibility of the constraints in the first run (left) and in the second one (right) of the iterative optimization procedure.

implemented to compute the critical load factor. Alternatively, accurate approximations could be found by performing eigenvalue analyses at suitable values of the load factor. In any case, the structural response of the optimal layouts retrieved by the proposed linear approach can be assessed by performing a finite element analysis including geometric nonlinearities. This allows for evaluating the bearing capacity, while checking that the deformation before buckling is relatively small.

3.2. A gridshell

A reticulated shell spanning a rectangular area with size $14\,\mathrm{m}\times 6\sqrt{3}\,\mathrm{m}$ is considered. The connectivity of the grid is that given in Fig. 10. The vertical load per unit of plan projection is $2.5\,\mathrm{kN/m^2}$. All the nodes along the perimeter are restrained in the three Cartesian axes.

The maximum allowed total length of the network is $l_{t,max} = 1.15 \cdot l_{t,0} = 563.5\,\mathrm{m}$, being $l_{t,0} = 490\,\mathrm{m}$ the total length of the members in the plane grid represented in Fig. 10. A profile of the type CHS 48.3/2.6 is assumed for all the branches of the reticulated shell, considering Young's modulus $E = 210$ GPa. The maximum allowed standard deviation of the element lengths is $l_{sd,max} = 0.10\,\mathrm{m}$.

At first, the formulation in Eq. (7) is used to search for the length-constrained minimum compliance design. The same approach described in Section 3.1 to deal with the design-dependent load is adopted, again starting from a uniform distribution of compressive stresses. The optimal layout found at the end of the multi-step procedure is that represented in Fig. 11 ($U_c = 72.38\,\mathrm{Nm}$), where maps of the forces at convergence are given. The degree of statically indeterminacy is 49, meaning that a large variety of statically admissible force distributions may be found for the geometry represented in the picture. The one retrieved from the adopted energy-based procedure coincides with that computed from the elastic solution under vertical loads. According to the plan view in Fig. 11(right), the optimal location of the nodes is different from that pertaining to a uniform distribution, as the hexagonal arrangement of Fig. 10. The achieved network of bars is an anti-funicular solution, with forces ranging between $s_{min} = -7.55\,\mathrm{kN}$ and $s_{max} = -0.33\,\mathrm{kN}$. The latter value is found in the branches that are almost parallel to the x axis, next to the perimeter of the bay; the former characterizes a few diagrid elements connecting the aforementioned longitudinal branches to the ground. The slenderness of the bars ranges between 40 and 85; the maximum utilization factor, considering the Perry-Robertson failure criteria with the same parameters of the previous example, is 0.12. When a linear buckling analysis is performed, a localized mode is found for the repeated eigenvalue $\lambda_c = \lambda_1 = \lambda_2 = 1.779$, which mainly involves the highly compressed diagrid members above mentioned, see Fig. 12. A very good agreement is found

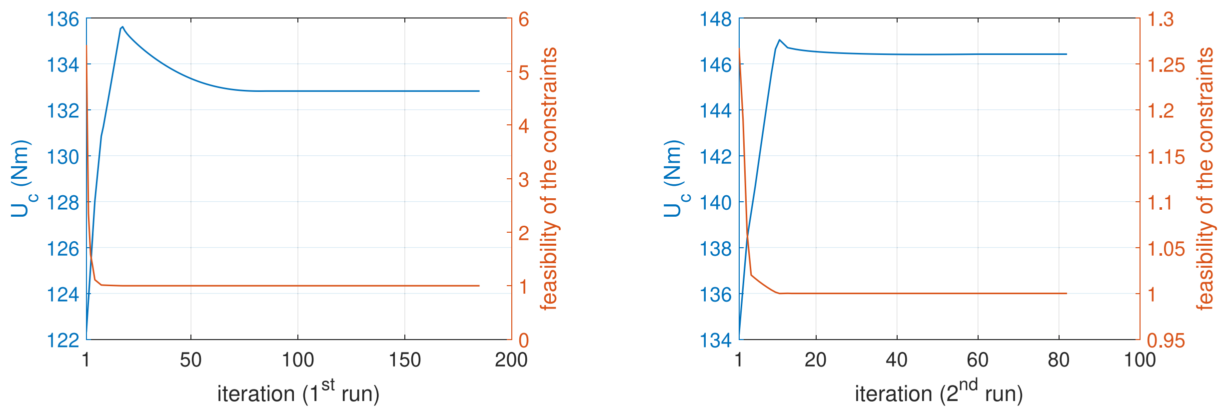

Fig. 9. Design of a dome for minimum compliance and $\lambda_{c,min} = 50$: history plot of the objective function and of the feasibility of the constraints in the first run (left) and in the second one (right) of the iterative optimization procedure.

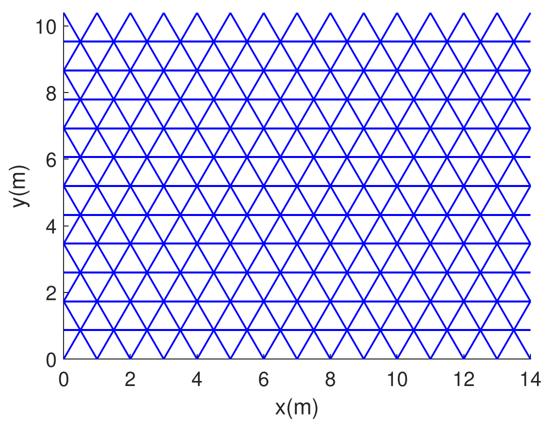

Fig. 10. Connectivity of the members of a gridshell.

looking at the eigenvalues retrieved by the proposed procedure and those computed via the commercial FEA software, see Table 2.

Then, the formulation in Eq. (15) is implemented, enforcing $\lambda_{c,min} = 15$ and using the previous solution as the starting guess. The optimal layout found at the end of the procedure to accommodate the design-dependent load is represented in Fig. 13 ($U_c = 92.41$ Nm). A color map is given for the forces in the branches, as computed from the values of the minimization unknowns at convergence. The achieved network comprises both bars in compression, with $s_{min} = -11.97$ kN and bars in tension $s_{max} = 3.48$ kN. The magnitude of s_{min} is 50% larger than in the previous design. However, the maximum utilization factor related to the Perry-Robertson failure criteria is less than 0.17. The maximum tensile force s_{max} arises along the longitudinal branches, next to the perimeter of the bay, thus improving the stiffness of the region nearby. Overall, the geometry of this gridshell is different from that of the reticulated shell represented Fig. 11. The corner zones are characterized by a peculiar design, as well as the aforementioned longitudinal branches whose curvature is more pronounced than in the previous case, see in particular Fig. 15. The critical load is approximately 8 times larger, and the relevant failure mode involves larger portions of the structure, see Fig. 14.

As already done for the dome in Section 3.1, the formulation endowed with the eigenvalue buckling constraint has been run using $\tilde{\mathbf{K}}_\sigma$ to approximate $\hat{\mathbf{K}}_\sigma$. Unlike the previous case, a difference has been found between the entries of $\mathbf{q}$ at convergence and the force densities in $\mathbf{q}_L$, which are computed as per Eq. (12) after a linear elastic solution. In the block of Table 2 that concerns the current example, the eigenvalues computed when implementing $\tilde{\mathbf{K}}_\sigma$ are given in the first row, within brackets, whereas those evaluated using the correct initial stress matrix are provided in the second. Values computed using $\hat{\mathbf{K}}_\sigma$ are in very good agreement with those retrieved via FEA by the commercial code. The bias in terms of critical load when using $\tilde{\mathbf{K}}_\sigma$ to approximate $\hat{\mathbf{K}}_\sigma$ is around 3%, see also discussions in [36,42] about the stress field in structures designed with elastic and plastic optimization approaches.

As expected, when the formulation in Eq. (15) is run implementing $\hat{\mathbf{K}}_\sigma$, a solution characterized by a final value of the strain energy that is slightly larger than that of the previous solution is retrieved ($U_c = 92.78$ Nm). The critical load multiplier is $\lambda_c = 15.382$. However, the achieved layout, the distribution of the elastic forces under the applied load, and the critical eigenmode look the same as those commented above.

In Fig. 16, history plots of the objective function and of the feasibility of the constraints are reported concerning the optimal solution in Fig. 13. Analogously to Section 3.1, the picture on the left refers to the first run of the iterative optimization procedure handling the design-dependent load vector, whereas that on the right relates to the second run. The former is initialized using the distribution of force densities in Fig. 11, whereas the latter is launched after an update of the tributary area of each node, starting from the previous solution. With respect to Figs. 8 and 9, a similar trend is found. However, the optimization of the gridshell is more demanding in terms of number of iterations.

3.3. A latticed column

A latticed column is addressed, inspired by the investigations presented in [67,68] in the field of Wire-and-Arc Additive Manufacturing (WAAM), see also [69,70]. Using the dot-by-dot deposition technique with a 304L stainless steel wire, bars with a diameter of 6 mm can be fabricated, having Young's modulus $E = 100$ GPa. A diagrid column with radius $r = 0.9/\pi$ m is herein investigated, considering a 996-bar structure, whose connectivity is represented in Fig. 17. The vertical load is applied at the top twelve nodes of the column, with a resultant of 10 kN. These top nodes are restrained along the x and y axes, whereas the twelve bottom nodes are restrained in the three Cartesian axes.

Throughout Section 3.3, the minimization of the strain energy is addressed implementing Eq. (8) instead of Eqs. (7c) and (15f), that means enforcing constraints on the minimum height of the top nodes of the column (for which $z_{i_c}^{min} = 2.5$ m is enforced), while disregarding the requirement on the maximum total length of the network. Unlike the previous examples, no ad hoc procedure to account for design-dependent loading is needed. Indeed, the loaded nodes are allowed to change their location only along the line of action of the applied force, with no effect on the equilibrium.

At first, the sensitivity of the minimum compliance layout with respect to the enforced maximum allowed standard deviation of the

Table 2
Design of a gridshell for minimum compliance and different assumptions on the enforcement of $\lambda_{c,min}$: values $\lambda_e = 1/\mu_e$ for $e = 1 \ldots n_e$ computed using the proposed method vs. FEA via commercial code (*in italic*).

Design	λ_1	λ_2	λ_3	λ_4	λ_5	λ_6
min U_c (Fig. 11)	1.779	1.779	3.738	3.738	5.232	5.236
	1.779	*1.779*	*3.739*	*3.739*	*5.234*	*5.238*
min U_c, $\lambda_{c,min} = 15$ (Fig. 13)	(15.207)	(15.207)	(15.631)	(15.692)	(15.781)	(15.788)
	14.848	14.848	15.354	15.507	15.818	15.868
	14.851	*14.851*	*15.364*	*15.517*	*15.834*	*15.891*

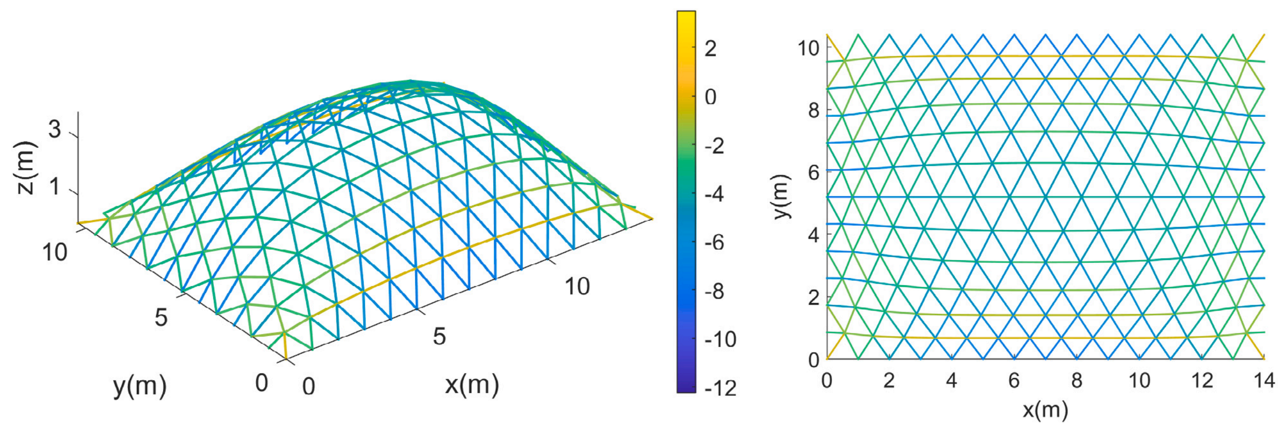

Fig. 11. Minimum compliance design of a gridshell ($U_c = 72.38$ Nm): optimal layout with map of the forces in the branches (in kN, $s_{min} = -7.55$ kN, $s_{max} = -0.33$ kN), in two views.

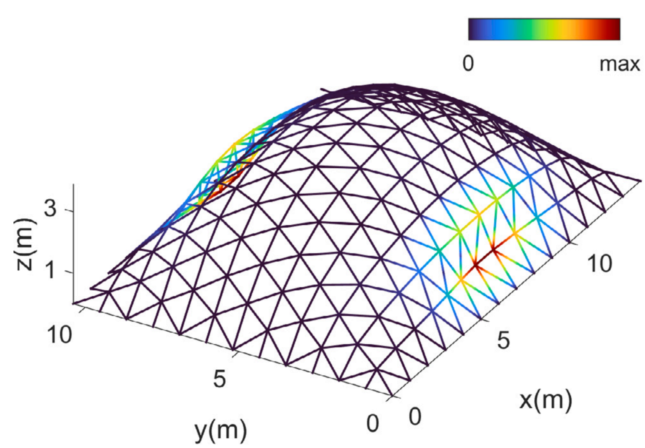

Fig. 12. Minimum compliance design of a gridshell: buckling mode at $\lambda_c = 1.779$.

element lengths is investigated. The optimization procedure in Eq. (7) is run for different values of $l_{sd,max}$, i.e. 0.005 m, 0.015 m, and 0.035 m. The algorithm is initialized by prescribing a homogeneous distribution of tensile force densities in the rings, and of compressive forces in all the remaining elements. The achieved optimal layouts are represented in Fig. 18, providing maps of the element forces due to the external loads. The degree of statically indeterminacy of the spatial networks is 13. At convergence, it has been checked that $\mathbf{q} = \mathbf{q}_L$.

The latticed elements share the height of the top nodes, but are characterized by different shapes, thus affecting the structural response. The larger the value $l_{sd,max}$, the smaller the strain energy at convergence, moving in the direction of a less constrained problem. Increasing $l_{sd,max}$ also implies a reduction of the peak forces, both in tension and in compression. However, allowing for larger variations in the element length, the slenderness of the bars remarkably grows at the ends of the column. Looking at the layout in Fig. 18(right), the complementary strain energy at convergence reads $U_c = 2.77$ Nm, which corresponds to a vertical displacement of the top nodes that is less than 0.6 mm. The slenderness of the elements ranges between 50 and 160. The maximum utilization factor, considering the Perry-Robertson failure criteria for a material with yielding stress $\sigma_y = 210$ GPa and lack of straightness of the jth bar equal to $3 \cdot 10^{-3} \cdot l_j$, see [31], is 0.45.

The critical load multiplier of this layout is extremely low. The eigenmode at $\lambda_c = 0.203$ is shown in Fig. 19, along with those corresponding to load multipliers that are close to the critical one. All of them involve limited portions of the lattice at the ends of the column, where the bars of largest slenderness are located.

The formulation in Eq. (15) is used to look for improved versions of the diagrid column in Fig. 18(right), i.e. that designed for $l_{sd,max} = 0.015$ m. The eigenvalue buckling constraint is implemented, working, first with $\lambda_{c,min} = 15$, and then with $\lambda_{c,min} = 50$. In both cases, the force densities that correspond to the design of Fig. 18(right) are used to initialize the algorithm. The optimal design found for $\lambda_{c,min} = 15$ is represented in Fig. 20, providing a map of the forces retrieved from the entries of $\mathbf{q}$ at convergence (coinciding with the values found via elastic equilibrium) and the critical eigenmode at $\lambda_{c,min} = 15.365$. This involves the entire latticed element. The achieved design is remarkably different with respect to that reported in Fig. 18(right). The diagrid size is graded more homogeneously along the length of the column, including the end regions, see also Fig. 22. This implies a reduction in the maximum value of the slenderness of the bar, ranging between 70 and 90. The diameter of the horizontal rings is larger than in the previous case. In this layout, it takes the minimum value at mid height of the column. The improved performance in terms of stability implies a 30% rise of complementary strain energy. A slight increase in the value of s_{min} and s_{max} is reported, too. However, due to the decrease in slenderness, the maximum utilization factor related to the Perry-Robertson failure criteria drops to 0.18.

The optimal layout found for $\lambda_{c,min} = 50$ is addressed in Fig. 21. The map of the forces computed using the entries of $\mathbf{q}$ at convergence matches the linear elastic solution, see Fig. 21(left). The critical eigenmode at $\lambda_{c,min} = 53.626$ involves the entire latticed element, see Fig. 21(right). The radius of the horizontal rings takes the maximum value at mid height, whereas the minimum is that prescribed at the ends of the column, see also Fig. 22. Indeed, the second moment of area of the circular hollow cross-section is remarkably large, see in

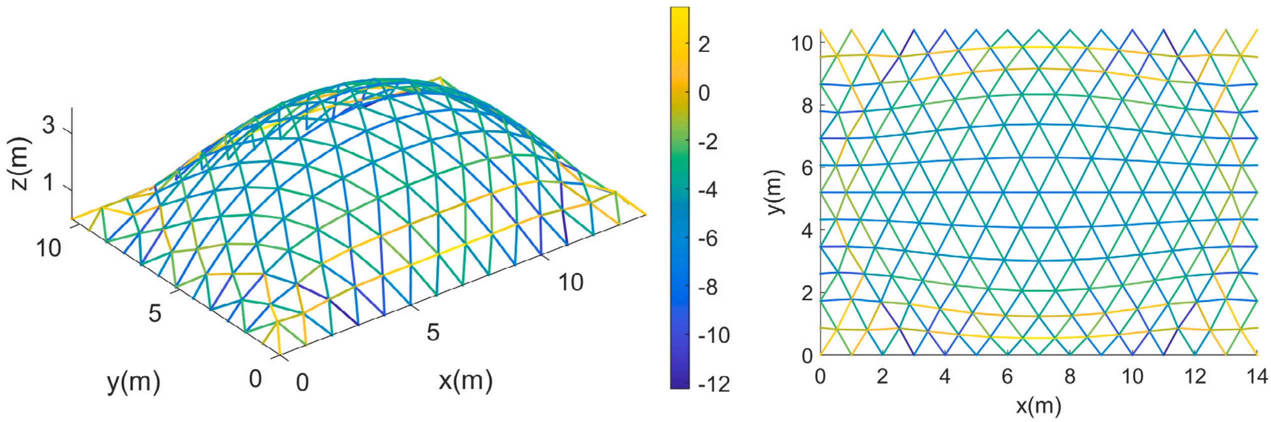

Fig. 13. Design of a gridshell for minimum compliance and $\lambda_{c,min} = 15$ ($U_c = 92.41$ Nm): optimal layout with map of the forces in the branches (in kN, $s_{min} = -11.97$ kN, $s_{max} = 3.48$ kN), in two views.

Table 3
Design of a latticed column for minimum compliance and different assumptions on the enforcement of $\lambda_{c,min}$: values $\lambda_e = 1/\mu_e$ for $e = 1 \dots n_e$ computed using the proposed method vs. FEA via commercial code (*in italic*).

Design	λ_1	λ_2	λ_3	λ_4	λ_5	λ_6
min U_c (Fig. 18)	0.203 *0.203*	0.203 *0.203*	0.392 *0.392*	0.392 *0.392*	0.583 *0.583*	0.583 *0.583*
min U_c, $\lambda_{c,min} = 15$ (Fig. 20)	15.365 *15.398*	15.365 *15.398*	15.413 *15.448*	15.413 *15.448*	15.417 *15.453*	15.417 *15.453*
min U_c, $\lambda_{c,min} = 50$ (Fig. 21)	53.626 *53.849*	53.626 *53.849*	53.635 *53.877*	53.778 *54.049*	54.021 *54.214*	54.206 *54.390*

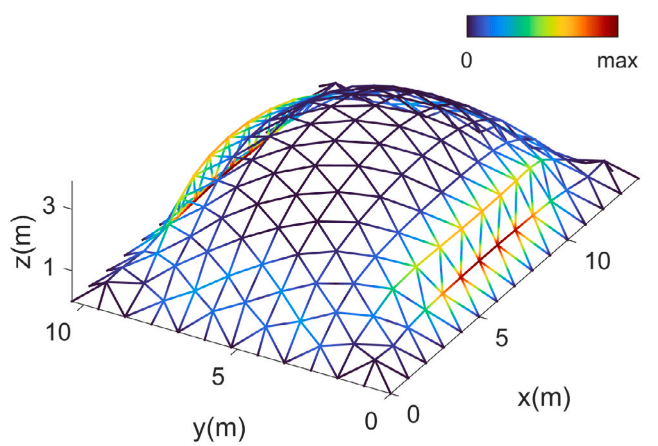

Fig. 14. Design of a gridshell for minimum compliance and $\lambda_{c,min} = 15$: buckling mode at $\lambda_c = 15.207$.

particular [71] dealing with the optimal design of concrete columns for additive manufacturing. The achievement on λ_c comes at the cost of a remarkable rise in terms of complementary strain energy, that, at convergence, is more than twice that of the design in Fig. 20. A further increase in the value of s_{min} and s_{max} is observed, mainly concerning the tensile forces in the rings. The largest value of bar slenderness raises to 150, whereas the maximum utilization factor related to the Perry-Robertson failure criteria is less than 0.25.

Both for $\lambda_{c,min} = 15$ and for $\lambda_{c,min} = 50$, the formulation in Eq. (15) has been run using $\tilde{\mathbf{K}}_\sigma$ to approximate $\hat{\mathbf{K}}_\sigma$. As already mentioned, at the end of each run, entries in $\mathbf{q}$ have been found to match the components of $\mathbf{q}_L$ in Eq. (12). A very good agreement may be reported looking also at Table 3, where the values $\lambda_e = 1/\mu_e$ provided by the implemented procedure are given along with those found using the commercial FEA code. The difference between pairs of values is less than 0.5%, similarly to what pointed out in Section 3.1.

In Fig. 23, history plots of the objective function and of the feasibility of the constraints are reported concerning the optimal solution in Fig. 20, on the left, and that in Fig. 21, on the right. It is recalled that, in both cases, a single optimization procedure is run, being the load vector design-independent. Also, the same starting guess is used, i.e. the set of force densities corresponding to the layout in Fig. 18(right). The curves are similar to those already presented in the previous sections. Notwithstanding the enforcement of a remarkable increase of $\lambda_{c,min}$ with respect to the starting guess, a limited number of iterations is reported.

4. Conclusions and ongoing research

A form-finding approach that is based on the force density method has been presented in this contribution to address the elastic design of reticulated shells. While most of the conventional approaches deal with plastic design, the complementary strain energy has been adopted in this contribution as objective function, formulating problems with constraints on the total length of the network or the location of a prescribed set of nodes. A global enforcement governing the standard deviation of the element lengths has been introduced to regularize the geometry of the network, thus preventing, although in a weak sense, uneven layouts in terms of bar slenderness. An eigenvalue buckling constraint has been embedded in the formulation to include stability considerations. In this regard, the approach presented in [43] dealing with topology optimization by distribution of isotropic material has been implemented herein in the context of form-finding. More in detail, a smooth aggregation function has been used to handle a few eigenvalues of the linear buckling problem with the aim of effectively controlling the critical load also in case of repeated or switching eigenvalues. The formalism of the force density method has been extensively used not only to manage the equilibrium equations, but also to assemble the stiffness matrix and the initial stress matrix. Since the minimization of the complementary energy goes in the direction of restoring compatibility, the adoption of the current set of force densities to approximate the stress regime has been tested as an option when constructing the latter matrix.

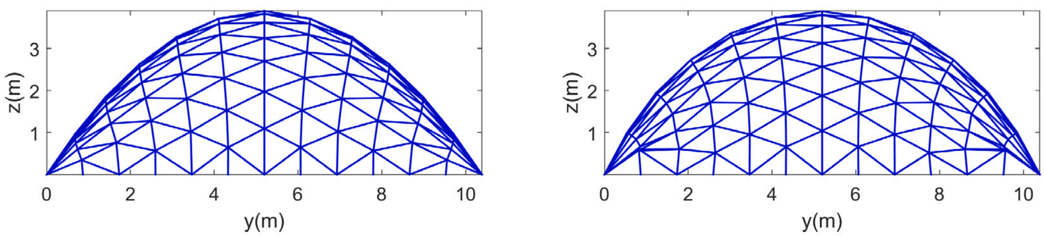

Fig. 15. Design of a gridshell for minimum compliance and different prescription on $\lambda_{c,min}$: side view of the optimal layout with no control of $\lambda_{c,min}$ (left) and for $\lambda_{c,min} = 15$ (right).

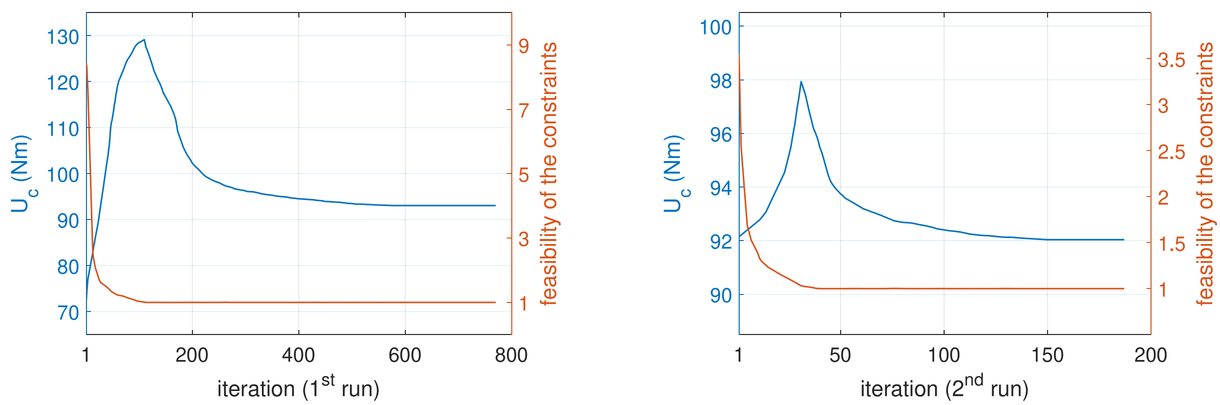

Fig. 16. Design of a gridshell for minimum compliance and $\lambda_{c,min} = 15$: history plot of the objective function and of the feasibility of the constraints in the first run (left) and in the second one (right) of the iterative optimization procedure.

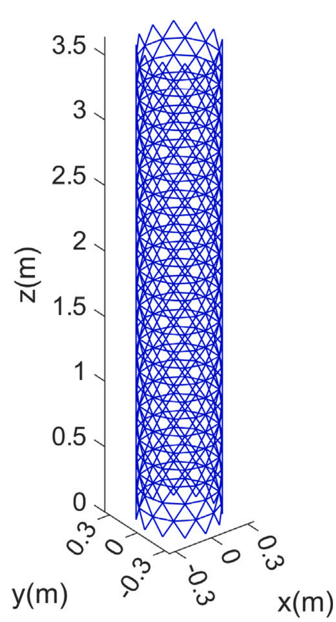

Fig. 17. Connectivity of the members for a diagrid column.

Numerical simulations have been addressed concerning the shape optimization of gridshells and stretching-dominated lattices. Given the grid connectivity, the bar cross-section, and the elastic modulus of the material, stiff spatial arrangements that fully satisfy the enforced constraints have been found. When disregarding stability considerations, optimal layouts are retrieved that may be prone to buckling issues. Critical eigenmodes have been found to affect either limited portions of the reticulated shell (see Sections 3.2 and 3.3), or more extended ones (see Section 3.1). The adoption of the eigenvalue buckling constraint has proved effective in raising the critical load multiplier at the cost of an increase in the objective function. This may be used e.g. to enforce the eigenvalue-based condition given by technical codes to rely on first order analyses in structural design. In general, the achieved optimal layouts take advantage of tensile-stressed elements. With respect to the design achieved while disregarding the eigenvalue buckling constraint, the largest magnitude of the compressive forces has been found to increase without remarkably affecting member buckling. A remarkable sensitivity of the optimal shape to the value of the enforced critical load multiplier has been reported.

Linear elastic and linear buckling analyses have been additionally performed by means of a commercial finite element code to provide a preliminary assessment of the achieved results. Overall, a very good agreement has been found. Minor differences have been reported for the example in Section 3.2, when adopting the approximated version of the initial stress matrix to deal with the eigenvalue buckling constraint.

Imperfections and possible interaction of buckling modes may remarkably affect the structural behavior of reticulated shells, see e.g. [8, 34]. The ongoing research is mainly concerned with an extension of the proposed procedure to account for defects and introduce eigenvalue separation, see in particular [72], considering applications at different scales, see also [73].

Experimental tests should be performed to assess the structural behavior of the optimal layouts designed by means of the proposed approach. Scaled models could be conveniently used for the reticulated shells in Sections 3.1 and 3.2, whereas full scale fabrication of the latticed columns in Section 3.3 using WAAM is currently under investigation, see [70].

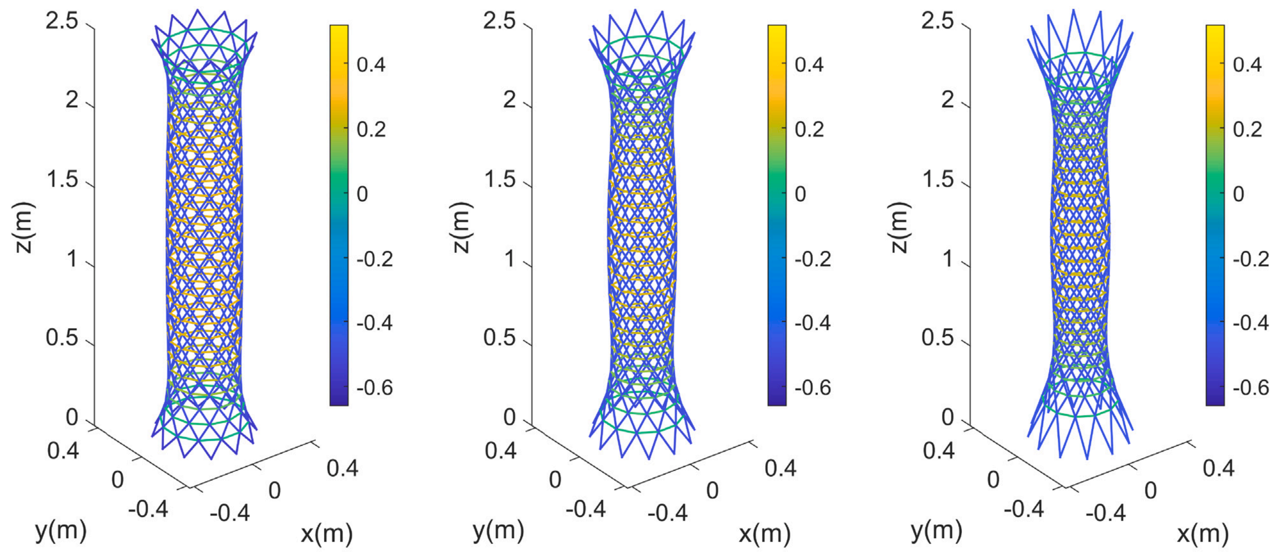

Fig. 18. Optimal layout and forces in the branches (in kN) for the minimum compliance design of a latticed column using different values of $l_{sd,max}$: 0.005 m (U_c = 3.36 Nm, $s_{min} = -0.56$ kN, $s_{max} = 0.26$ kN, left) 0.015 m (U_c = 3.01 Nm, $s_{min} = -0.50$ kN, $s_{max} = 0.24$ kN, center), 0.035 m (U_c = 2.77 Nm, $s_{min} = -0.48$ kN, $s_{max} = 0.23$ kN, right).

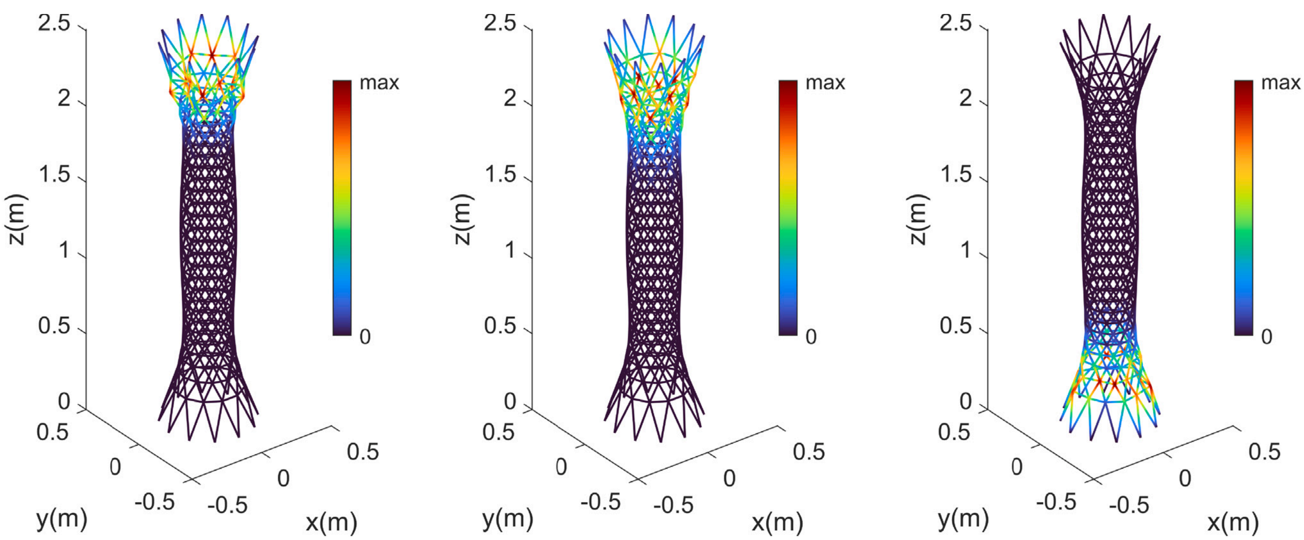

Fig. 19. Eigenmodes associated to the load multipliers $\lambda_c = \lambda_1 = 0.203$ (left), $\lambda_3 = 0.392$ (center), and $\lambda_5 = 0.583$ (right) for the minimum compliance design of a latticed column using $l_{sd,max} = 0.035$ m. The color maps represent the amplitude of the eigenmodes.

CRediT authorship contribution statement

Matteo Bruggi: Supervision, Software, Methodology, Funding acquisition, Conceptualization. **Carlo Guerini:** Investigation, Formal analysis, Data curation.

Declaration of competing interest

The authors declare that they have no known competing financial interests or personal relationships that could have appeared to influence the work reported in this paper.

Acknowledgments

Funded by the European Union - Next Generation EU, Mission 4, Component 1, CUP D53D23003900006, PRIN 2022P7FLNC "LATTICE" (Lattice meso-elements for a new class of green steel structures).

Appendix. Sensitivity computation

In [9], the sensitivity computation with respect to the vector of the minimization variables $\mathbf{q}$ was originally provided for the vectors gathering the coordinates of the nodes, $\mathbf{x}$, $\mathbf{y}$, $\mathbf{z}$, and the length of the bars, $\mathbf{l}$. Addressing Eq. (3) as $\mathbf{C}_x^T\mathbf{U}\mathbf{q} = \mathbf{p}_x$, $\mathbf{C}_y^T\mathbf{V}\mathbf{q} = \mathbf{p}_y$, $\mathbf{C}_z^T\mathbf{W}\mathbf{q} = \mathbf{p}_z$, and enforcing that any changes $d\mathbf{q}$, $d\mathbf{x}$, $d\mathbf{y}$, and $d\mathbf{z}$ do not affect the state of equilibrium, one has:

$$\frac{\partial \mathbf{x}}{\partial \mathbf{q}} = -(\mathbf{C}_x^T\mathbf{Q}\mathbf{C}_x)^{-1}\mathbf{C}_x^T\mathbf{U}, \quad \frac{\partial \mathbf{y}}{\partial \mathbf{q}} = -(\mathbf{C}_y^T\mathbf{Q}\mathbf{C}_y)^{-1}\mathbf{C}_y^T\mathbf{V},$$
$$\frac{\partial \mathbf{z}}{\partial \mathbf{q}} = -(\mathbf{C}_z^T\mathbf{Q}\mathbf{C}_z)^{-1}\mathbf{C}_z^T\mathbf{W}, \tag{A.1}$$

where $\partial\mathbf{u}/\partial\mathbf{x} = \mathbf{C}_x$, $\partial\mathbf{v}/\partial\mathbf{y} = \mathbf{C}_y$, $\partial\mathbf{w}/\partial\mathbf{z} = \mathbf{C}_z$ were used, see Eq. (2). The assumption of design-independent loads holds. Hence:

$$\frac{\partial \mathbf{l}}{\partial \mathbf{q}} = \frac{\partial \mathbf{l}}{\partial \mathbf{x}}\frac{\partial \mathbf{x}}{\partial \mathbf{q}} + \frac{\partial \mathbf{l}}{\partial \mathbf{y}}\frac{\partial \mathbf{y}}{\partial \mathbf{q}} + \frac{\partial \mathbf{l}}{\partial \mathbf{z}}\frac{\partial \mathbf{z}}{\partial \mathbf{q}} = \mathbf{L}^{-1}\mathbf{U}\mathbf{C}_x\frac{\partial \mathbf{x}}{\partial \mathbf{q}} + \mathbf{L}^{-1}\mathbf{V}\mathbf{C}_y\frac{\partial \mathbf{y}}{\partial \mathbf{q}} + \mathbf{L}^{-1}\mathbf{W}\mathbf{C}_z\frac{\partial \mathbf{z}}{\partial \mathbf{q}}. \tag{A.2}$$

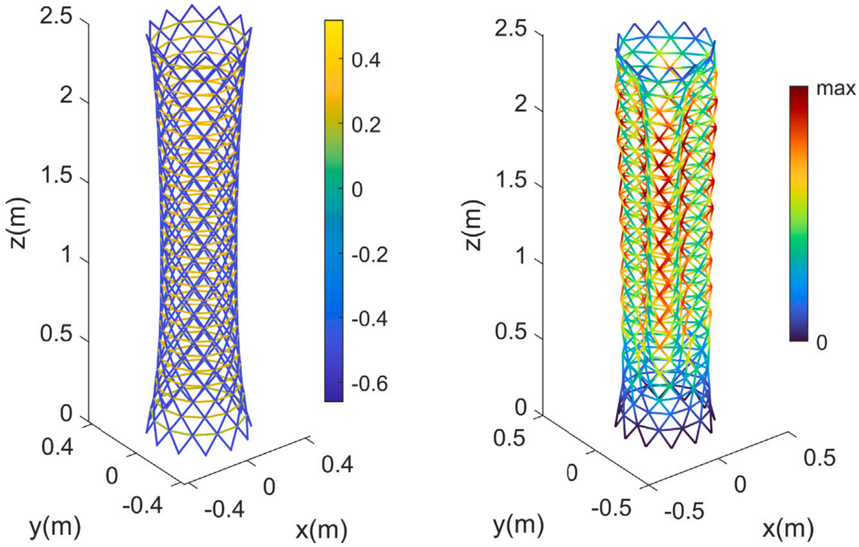

Fig. 20. Design of a latticed column for minimum compliance and $\lambda_{c,min}$ = 15 (U_c = 3.62 Nm): optimal layout with map of the force in the branches (in kN, s_{min} = −0.55 kN, s_{max} = 0.27 kN, left); relevant buckling mode at λ_c = 15.365 (right).

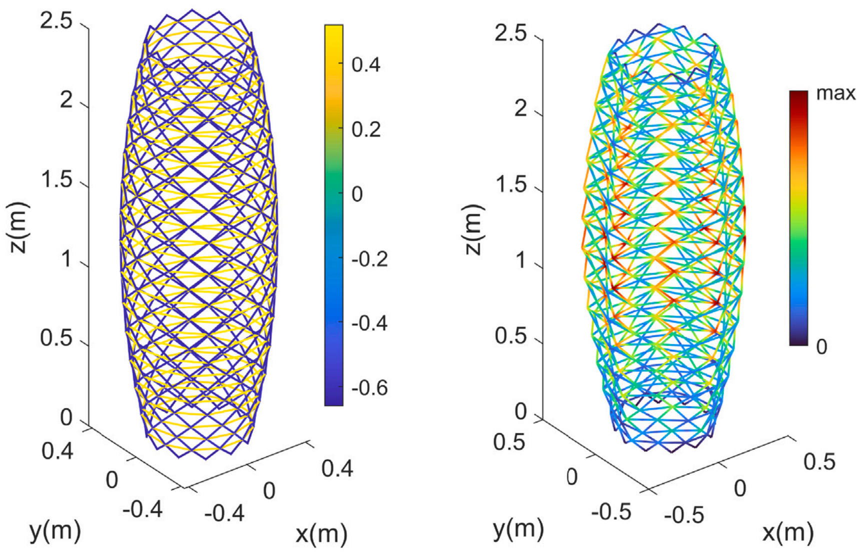

Fig. 21. Design of a latticed column for minimum compliance and $\lambda_{c,min}$ = 50 (U_c = 8.91 Nm): optimal layout with map of the force in the branches (in kN, s_{min} = −0.65 kN, s_{max} = 0.51 kN, left); relevant buckling mode at λ_c = 53.626 (right).

The derivatives of the complementary strain energy can be found analogously. By applying the product rule to the last member of Eq. (6) and accounting for $\mathbf{L}^3\mathbf{q} = \mathbf{Q}\mathbf{l}^3$, one gets:

$$\frac{\partial U_c}{\partial \mathbf{q}} = \frac{1}{2EA}\left(2\mathbf{L}^3\mathbf{q} + 3\mathbf{L}^2\frac{\partial \mathbf{l}}{\partial \mathbf{q}}\mathbf{q}\right). \tag{A.3}$$

Concerning the constraint in Eqs. (7c) and (15f), the vector of the sensitivity of the total length with respect to $\mathbf{q}$ can be computed by summing the components of the Jacobian matrix in Eq. (A.2) along the columns. To address the constraint in Eqs. (7d) and (15g), one has to account that $\partial(\mathbf{l}^T\mathbf{l})/\partial\mathbf{q} = 2\mathbf{l}^T\partial\mathbf{l}/\partial\mathbf{q}$.

Dealing with critical loads, the derivative of Eq. (14) with respect to the kth minimization unknown may be computed as [43]:

$$\frac{\partial J_{KS}(\boldsymbol{\mu})}{\partial q_k} = \frac{\sum_{e=1}^{n_e} e^{\rho(\mu_e-\mu_1)}\frac{\partial \mu_e}{\partial q_k}}{\sum_{e=1}^{n_e} e^{\rho(\mu_e-\mu_1)}}. \tag{A.4}$$

In the above equation, the derivative of the e-the eigenvalue with respect to q_k is found as [54]:

$$\frac{\partial \mu_e}{\partial q_k} = -\left[\boldsymbol{\Phi}_e^T\frac{\partial \hat{\mathbf{K}}_\sigma}{\partial q_k}\boldsymbol{\Phi}_e + \mu_e\boldsymbol{\Phi}_e^T\frac{\partial \mathbf{K}_L}{\partial q_k}\boldsymbol{\Phi}_e\right] + \bar{\mathbf{d}}_{L,e}^T\frac{\partial \mathbf{K}_L}{\partial q_k}\mathbf{d}_L, \tag{A.5}$$

where $\bar{\mathbf{d}}_{L,e}$ is the solution of the adjoint problem:

$$\mathbf{K}_L\bar{\mathbf{d}}_{L,e} = \frac{\partial \hat{\mathbf{K}}_\sigma}{\partial \mathbf{d}_L}\boldsymbol{\Phi}_e. \tag{A.6}$$

The solution of n_e additional problems of the type in Eq. (A.6) is needed to account for the dependence of the initial stress matrix on $\mathbf{d}_L$. The sensitivity of $\mathbf{K}_L$ with respect to q_k may be computed by differentiation of Eq. (10). The derivatives of $\hat{\mathbf{K}}_\sigma$ with respect to q_k and $\mathbf{d}_L$ are evaluated considering both Eqs. (11) and (12).

When $\tilde{\mathbf{K}}_\sigma$ is used as an approximation of $\hat{\mathbf{K}}_\sigma$, see Section 2.4, Eq. (A.5) takes a form similar to that used for natural frequencies. Such a problem involves the stiffness matrix and the mass matrix, the latter

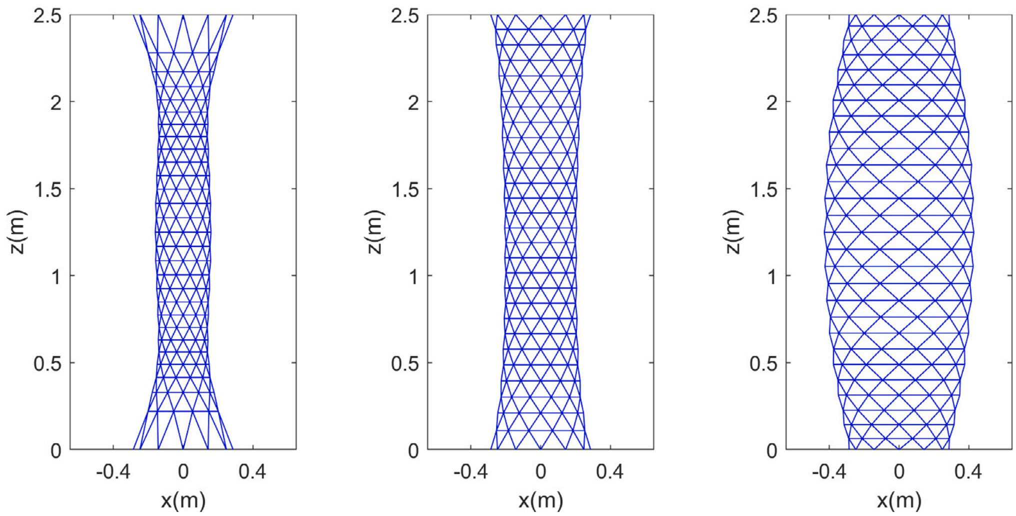

Fig. 22. Design of a latticed column for minimum compliance and different prescription on $\lambda_{c,min}$: side view of the optimal layout with no control of $\lambda_{c,min}$ (left), for $\lambda_{c,min} = 15$ (center) and for $\lambda_{c,min} = 50$ (right).

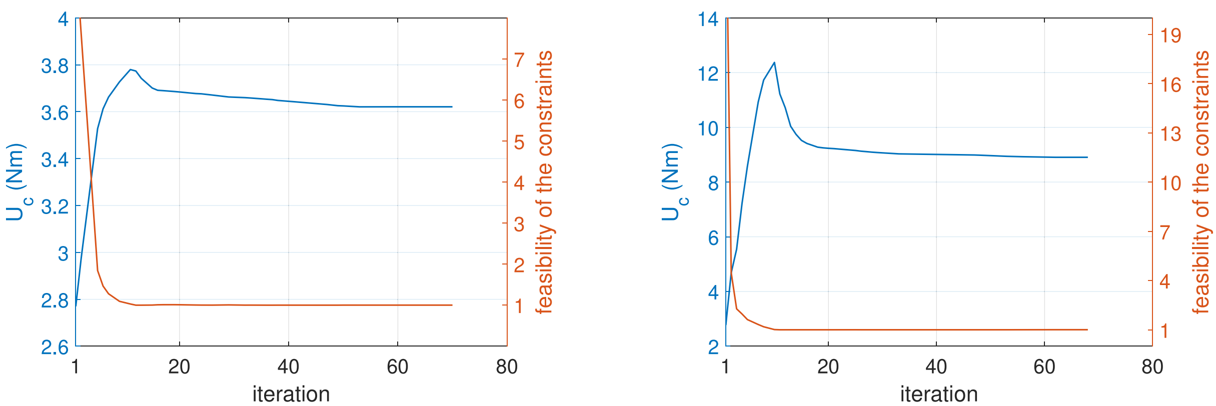

Fig. 23. Design of a latticed column for minimum compliance and different prescription on $\lambda_{c,min}$: history plot of the objective function and of the feasibility of the constraints for $\lambda_{c,min} = 15$ (left) and for $\lambda_{c,min} = 50$ (right).

depending solely on the minimization unknowns, see e.g. [72]. Hence, in Eq. (A.5) only the term in bracket is computed, meaning that no additional adjoint problem has to be solved. Moreover, the derivative of $\tilde{\mathbf{K}}_\sigma$ with respect to q_k is evaluated considering $\mathbf{q}_L = \mathbf{q}$ in Eq. (11).

Data availability

No unreferenced data are required. To facilitate replication of results, the manuscript discusses the formulations in detail and provides the input parameters used to run the numerical examples.

References

[1] Adriaenssens S, Block P, Veenendaal D, Williams CJK. Shell structures for architecture: Form finding and optimization. Routledge; 2014.

[2] Moskaleva A, Gusev S, Konev S, Sergeichev I, Safonov A, Hernandez-Montes E. Composite freeform shell structures: Design, construction and testing. Compos Struct 2023;306:116603.

[3] Winslow P, Pellegrino S, Sharma SB. Multi-objective optimization of free-form grid structures. Struct Multidiscip Optim 2010;40(1–6):257–69.

[4] Veenendaal D, Block P. An overview and comparison of structural form finding methods for general networks. Int J Solids Struct 2012;49(26):3741–53.

[5] Richardson JN, Adriaenssens S, Filomeno Coelho R, Bouillard P. Coupled form-finding and grid optimization approach for single layer grid shells. Eng Struct 2013;52:230–9.

[6] Jiang Y, Zegard T, Baker WF, Paulino GH. Form-finding of grid-shells using the ground structure and potential energy methods: a comparative study and assessment. Struct Multidiscip Optim 2018;57(3):1187–211.

[7] Rombouts J, Lombaert G, De Laet L, Schevenels M. A novel shape optimization approach for strained gridshells: Design and construction of a simply supported gridshell. Eng Struct 2019;192:166–80.

[8] Manuello A. Multi-body rope approach for grid shells: Form-finding and imperfection sensitivity. Eng Struct 2020;221:111029.

[9] Schek H. The force density method for form finding and computation of general networks. Comput Methods Appl Mech Engrg 1974;3(1):115–34.

[10] Liew A, Avelino R, Moosavi V, Van Mele T, Block P. Optimising the load path of compression-only thrust networks through independent sets. Struct Multidiscip Opt 2019;60(1):231–44.

[11] Vassart N, Motro R. Multiparametered formfinding method: application to tensegrity systems. Int J Space Struct 1999;14(2):147–54.

[12] Zhang J, Ohsaki M. Adaptive force density method for form-finding problem of tensegrity structures. Int J Solids Struct 2006;43(18–19):5658–73.

[13] Xu X, Wang Y, Luo Y. Finding member connectivities and nodal positions of tensegrity structures based on force density method and mixed integer nonlinear programming. Eng Struct 2018;166:240–50.

[14] Zhang L-Y, Zhu S-X, Li S-X, Xu G-K. Analytical form-finding of tensegrities using determinant of force-density matrix. Compos Struct 2018;189:87–98.

[15] Cai J, Wang X, Deng X, Feng J. Form-finding method for multi-mode tensegrity structures using extended force density method by grouping elements. Compos Struct 2018;187:1–9.

[16] Descamps B, Filomeno Coelho R, Ney L, Bouillard P. Multicriteria optimization of lightweight bridge structures with a constrained force density method. Comput Struct 2011;89(3–4):277–84.

[17] Yuan S, Yang B. The fixed nodal position method for form finding of high-precision lightweight truss structures. Int J Solids Struct 2019;161:82–95.

[18] Morterolle S, Maurin B, Quirant J, Dupuy C. Numerical form-finding of geotensoid tension truss for mesh reflector. Acta Astronaut 2012;76:154–63.

[19] Malerba PG, Patelli M, Quagliaroli M. An extended force density method for the form finding of cable systems with new forms. Struct Eng Mech 2012;42(2):191–210.
[20] Pauletti RMO, Pimenta PM. The natural force density method for the shape finding of taut structures. Comput Methods Appl Mech Engrg 2008;197(49–50):4419–28.
[21] Block P, Lachauer L. Three-dimensional funicular analysis of masonry vaults. Mech Res Commun 2014;56:53–60.
[22] Liew A, Pagonakis D, Van Mele T, Block P. Load-path optimisation of funicular networks. Meccanica 2018;53(1–2):279–94.
[23] Baker WF, Beghini LL, Mazurek A, Carrion J, Beghini A. Maxwell's reciprocal diagrams and discrete Michell frames. Struct Multidiscip Optim 2013;48(2):267–77.
[24] Liew A. Constrained force density method optimisation for compression-only shell structures. Structures 2020;28:1845–56.
[25] Bruggi M. A constrained force density method for the funicular analysis and design of arches, domes and vaults. Int J Solids Struct 2020;193–194:251–69.
[26] Christensen PW, Klarbring A. An introduction to structural optimization, vol. 153. Solid mechanics and its applications, Dordrecht, Netherlands: Springer; 2008, p. 1–220.
[27] Svanberg K. The method of moving asymptotes—a new method for structural optimization. Internat J Numer Methods Engrg 1987;24(2):359–73.
[28] Giraldo-Londoño O, Paulino GH. Polystress: a matlab implementation for local stress-constrained topology optimization using the augmented Lagrangian method. Struct Multidiscip Optim 2021;63(4):2065–97.
[29] Montemurro M, Bertolino G, Roiné T. A general multi-scale topology optimisation method for lightweight lattice structures obtained through additive manufacturing technology. Compos Struct 2021;258:113360.
[30] Yi B, Zhou Y, Yoon GH, Saitou K. Topology optimization of functionally-graded lattice structures with buckling constraints. Comput Methods Appl Mech Engrg 2019;354:593–619.
[31] Bruggi M, Laghi V, Trombetti T. Stress-based form-finding of gridshells for wire-and-arc additive manufacturing considering overhang constraints. Eng Struct 2023;279:115654.
[32] Bendsøe MP, Ben-Tal A, Zowe J. Optimization methods for truss geometry and topology design. Struct Optim 1994;7(3):141–59.
[33] Ohsaki M, Hayashi K. Force density method for simultaneous optimization of geometry and topology of trusses. Struct Multidiscip Optim 2017;56(5):1157–68.
[34] Gioncu V. Buckling of reticulated shells: State-of-the-art. Int J Space Struct 1995;10(1):1–46.
[35] Bulenda T, Knippers J. Stability of grid shells. Comput Struct 2001;79(12):1161–74.
[36] Descamps Bt, Filomeno Coelho R. The nominal force method for truss geometry and topology optimization incorporating stability considerations. Int J Solids Struct 2014;51(13):2390–9.
[37] Pedersen NL, Nielsen AK. Optimization of practical trusses with constraints on eigenfrequencies, displacements, stresses, and buckling. Struct Multidiscip Optim 2003;25(5–6):436–45.
[38] Ben-Tal A, Jarre F, Kočvara M, Nemirovski A, Zowe J. Optim Eng 2000;1(2):189–213.
[39] Weldeyesus AG, Gondzio J, He L, Gilbert M, Shepherd P, Tyas A. Truss geometry and topology optimization with global stability constraints. Struct Multidiscip Optim 2020;62(4):1721–37.
[40] Shen W, Ohsaki M, Yamakawa M. Robust geometry and topology optimization of plane frames using order statistics and force density method with global stability constraint. Internat J Numer Methods Engrg 2021;122(14):3653–77.
[41] Saka MP. Optimum topological design of geometrically nonlinear single layer latticed domes using coupled genetic algorithm. Comput Struct 2007;85(21–22):1635–46.
[42] Kirsch U. On singular topologies in optimum structural design. Struct Optim 1990;2(3):133–42.
[43] Ferrari F, Sigmund O, Guest JK. Topology optimization with linearized buckling criteria in 250 lines of Matlab. Struct Multidiscip Optim 2021;63(6):3045–66.
[44] CEN. Eurocode 3: Design of steel structures. EN 1993-1-1 2005.
[45] He S-S, Yin X, Zhang L-Y, Gao Z-Y, Xu G-K. Directional snapping instability in a bistable tensegrity under uniaxial loads. Compos Struct 2022;283:115153.
[46] Guerra Riaño AF, Várkonyi PL. Form-finding using the force density method: Existence of solutions, singularities, and an analogy to electric circuits. Int J Space Struct 2023;38(4):302–26.
[47] Jewett JL, Carstensen JV. Experimental investigation of strut-and-tie layouts in deep RC beams designed with hybrid bi-linear topology optimization. Eng Struct 2019;197:109322.
[48] Xia Y, Langelaar M, Hendriks MAN. Optimization-based strut-and-tie model generation for reinforced concrete structures under multiple load conditions. Eng Struct 2022;266(114501):114501.
[49] Najian Asl R, Bletzinger K-U. The implicit bulk-surface filtering method for node-based shape optimization and a comparison of explicit and implicit filtering techniques. Struct Multidiscip Optim 2023;66(5).
[50] Swartz K, Mittal K, Schmidt M, Barrera J, Watts S, Tortorelli D. Yet another parameter-free shape optimization method. Struct Multidiscip Optim 2023;66(12).
[51] Westergaard H. On the method of complementary energy. Trans Am Soc Civil Eng 1942;107(1):765–93.
[52] Wriggers P. Nonlinear finite element methods. Heidelberg: Springer Berlin; 2008.
[53] Zhang J, Ohsaki M. Tensegrity structures: Form, stability, and symmetry. Heidelberg: Springer Tokyo; 2015.
[54] Rodrigues HC, Guedes JM, Bendsø e MP. Necessary conditions for optimal design of structures with a nonsmooth eigenvalue based criterion. Struct Optim 1995;9(1):52–6.
[55] Kreisselmeier G, Steinhauser R. Systematic control design by optimizing a vector performance index. In: Computer aided design of control systems. Elsevier; 1980, p. 113–7.
[56] Gravesen J, Evgrafov A, Nguyen DM. On the sensitivities of multiple eigenvalues. Struct Multidiscip Optim 2011;44(4):583–7.
[57] Seyranian AP, Lund E, Olhoff N. Multiple eigenvalues in structural optimization problems. Struct Optim 1994;8(4):207–27.
[58] Aita D, Bruggi M. A numerical method for the funicular analysis of masonry vaults accounting for stereotomy, finite strength and finite friction. Eng Struct 2023;293:116658.
[59] Dillen W, Lombaert G, Schevenels M. A hybrid gradient-based/metaheuristic method for Eurocode-compliant size, shape and topology optimization of steel structures. Eng Struct 2021;239:112137.
[60] Raspanti CG, Bandoni JA, Biegler LT. New strategies for flexibility analysis and design under uncertainty. Comput Chem Eng 2000;24(9–10). 2193–2209.
[61] Gythiel W, Mommeyer C, Raymaekers T, Schevenels M. A comparative study of the structural performance of different types of reticulated dome subjected to distributed loads. Front Built Environ 2020;6.
[62] Lewiński T, Sokół T, Graczykowski C. Michell structures. Cham: Springer; 2019.
[63] Meng L, Zhang J, Hou Y, Breitkopf P, Zhu J, Zhang W. Revisiting the fibonacci spiral pattern for stiffening rib design. Int J Mech Sci 2023;246:108131.
[64] Strand7, Release 3, 2021, The MathWorks Inc., URL www.strand7.com/r3.
[65] Krenk S, Høgsberg J. Statics and mechanics of structures. Dordrecht: Springer; 2013.
[66] Dunning P. Stability constraints for geometrically nonlinear topology optimization. Struct Multidiscipl Optim 2023;66:253.
[67] Laghi V, Palermo M, Gasparini G, Trombetti T. Computational design and manufacturing of a half-scaled 3D-printed stainless steel diagrid column. Addit Manuf 2020;36(101505):101505.
[68] Yu Z, Pan Z, Ding D, Polden J, He F, Yuan L, Li H. A practical fabrication strategy for wire arc additive manufacturing of metallic parts with wire structures. J Adv Manuf Technol 2021;115(9–10):3197–212.
[69] Huang C, Kyvelou P, Gardner L. Stress-strain curves for wire arc additively manufactured steels. Eng Struct 2023;279:115628.
[70] Costello SCA, Cunningham CR, Xu F, Shokrani A, Dhokia V, Newman ST. The state-of-the-art of wire arc directed energy deposition (WA-DED) as an additive manufacturing process for large metallic component manufacture. Int J Comput Integr 2023;36(3):469–510.
[71] Mogra M, Asaf O, Sprecher A, Amir O. Design optimization of 3D printed concrete elements considering buildability. Eng Struct 2023;294:116735.
[72] Jensen JS, Pedersen NL. On maximal eigenfrequency separation in two-material structures: the 1D and 2D scalar cases. J Sound Vib 2006;289(4–5):967–86.
[73] Liu H, Chen L, Jiang Y, Zhu D, Zhou Y, Wang X. Multiscale optimization of additively manufactured graded non-stochastic and stochastic lattice structures. Compos Struct 2023;305:116546.